nature communications

Article

https://doi.org/10.1038/s41467-025-60832-z

An orally available M^{pro}/TMPRSS2 bispecific inhibitor with potent anti-coronavirus efficacy in vivo

Received: 14 November 2024

Accepted: 5 June 2025

Huiping Shuai[1,16], Jingxin Qiao[2,16], Chaemin Yoon[1,16], Guo Zhang[2,16], Yuxin Hou[3,4,16], Xiaoyan Xia[2,16], Lei Wang[1,16], Xinyue Deng[2,16], Yifei Wang[2], Qingquan Li[5,6], Lianzhao Du[1], Yuanchen Liu[1], Minmin Zhou[1], Hoi Ting Wong[1], Jiaheng Hu[1], Huan Liu[1], Bingjie Hu[1], Dong Wang[7], Jingyi Su[8], Yuying Pan[8], Yongtao Ye[9], Yan Chen[2], Zhen Fang[2], Ziyi Xia[2], Yue Chai[1], Jialu Shi[1], Yang Wang[1], Tianrenzheng Zhu[1], Honglei Zhang[1,10], Shuofeng Yuan[1,11,12], Jie Zhou[1,11], Jasper Fuk-Woo Chan[1,3,11,12,13,14], Kwok-Yung Yuen[1,3,11,12,13,14], Chunfu Xu[5,6], Jian Lei[2] ✉, Shengyong Yang[2] ✉ & Hin Chu[1,11,12,15] ✉

Coronaviruses have caused three major endemics in the past two decades. Alarmingly, recent identification of novel zoonotic coronaviruses that caused human infections suggests the risk of future coronavirus outbreak caused by spillover infection from animal reservoirs remains high. Therefore, development of alternative therapeutic options with broad-spectrum anti-coronavirus activities are urgently needed. Here, we develop an orally available bispecific inhibitor, TMP1, which simultaneously targets key coronavirus replication protease M^{pro} and the essential airway protease TMPRSS2. TMP1 shows broad-spectrum protection not only against different SARS-CoV-2 variants but also against multiple human-pathogenic coronaviruses in vitro. By using the K18-hACE2 transgenic mouse, hDPP4 knock-in mouse and golden Syrian hamster models, we demonstrate TMP1 cross-protects against highly-pathogenic coronaviruses (SARS-CoV-1, SARS-CoV-2 and MERS-CoV) in vivo and efficiently abrogates SARS-CoV-2 transmission. Through structural and mutagenesis studies, we confirm the direct interaction of TMP1 with M^{pro} and TMPRSS2, and pinpoint the key sites of interactions. Importantly, TMP1 inhibits the infection of nirmatrelvir-resistant SARS-CoV-2 escape mutants. Together, our findings demonstrate the antiviral potential of the bispecific M^{pro}/TMPRSS2 antiviral design against human-pathogenic coronaviruses and other emerging coronaviruses.

Coronavirus infections have long been prevalent in the human population. Apart from the four endemic human coronaviruses (HCoV-229E, -NL63, -OC43 and -HKU1)[1], the highly pathogenic severe acute respiratory syndrome coronavirus (SARS-CoV-1) and Middle East respiratory syndrome coronavirus (MERS-CoV) have caused major outbreaks manifested with severe viral pneumonia[2,3]. In 2019, severe acute respiratory syndrome coronavirus 2 (SARS-CoV-2) emerged and have resulted in the global coronavirus disease 2019 (COVID-19) pandemic, which has accounted for over seven million deaths worldwide to date[4,5]. Moreover, recent identification of the porcine deltacoronavirus (Hu-PDCoV) in children and the canine coronavirus human pneumonia 2018 (CCoV-HuPn-2018)[6,7] alarmingly underscored

A full list of affiliations appears at the end of the paper. ✉e-mail: leijian@scu.edu.cn; yangsy@scu.edu.cn; hinchu@hku.hk

the increasing possibility of coronavirus spillover to infect humans. Given the current situation, the chance of future emergence of zoonotic coronaviruses remains high. To prepare for the emerging coronavirus outbreaks, development of effective therapeutic options with pan-coronavirus efficacy are urgently needed.

Coronavirus entry mediated by the spike (S) protein is the first step to establish successful virus infection. To mediate efficient coronavirus entry, sequential cleavage of coronavirus S protein at the S1/S2 and the S2′ site by host proteases is essential. Although recent evidence suggested that a variety of transmembrane proteases could facilitate S protein cleavage[8,9], TMPRSS2 is predominantly used by coronaviruses to mediate virus entry at the plasma membrane[10–14]. Alternatively, coronavirus entry can take place in the endosomes that requires cathepsin B/L[15]. A wealth of studies has therefore developed anti-coronavirus host-directed antivirals (HDAs) based on these important host proteases[15–17]. Blockade of the endosomal entry pathway sufficiently aborted coronavirus infection in cells with little to no TMPRSS2 expression[15,18]. Yet in the airway epithelium where abundant TMPRSS2 is expressed[14,19], TMPRSS2-dependent virus entry remains as the dominant pathway utilized by human-pathogenic coronaviruses[10–14,20–23]. In addition, TMPRSS2 is a key determinant that impacts coronavirus transmission and virus-induced tissue pathologies in the infected host[24–26], suggesting the indispensable role of TMPRSS2 to coronavirus entry and pathogenesis at the primary infection sites.

After coronavirus entry into the host cell, its positive-sense RNA genome is translated into two long viral polypeptides pp1a and pp1ab. The viral main protease (M^{pro}) is a cysteine protease that is responsible for the release of 12 out of the 16 replicases vital to virus replication by enzymatic cleavage of pp1a and pp1ab[27,28]. Resolution of the M^{pro} crystal structures of coronaviruses demonstrated that their 3D structures were highly conserved[29]. Interestingly, M^{pro} specifically recognizes a glutamine residue at the P1 position of the substrate, which is a unique feature that is not shared by any of the host cysteine protease[30,31]. Therefore, M^{pro} has been an attractive antiviral target for the development of anti-coronavirus therapy[32–35].

Here, we describe an orally available M^{pro}/TMPRSS2 bispecific inhibitor, TMP1, which simultaneously targets coronavirus entry and replication with potent pan-coronavirus antiviral efficacy both in vitro and in vivo. Notably, we show that TMP1 prevents severe infection in the lower respiratory tract, rescues lethal SARS-CoV-2 infection, and blocks coronavirus transmission. Furthermore, we reveal a differential mode of action of TMP1 when compared to nirmatrelvir, which effectively protects the host from infection of nirmatrelvir-resistant SARS-CoV-2 mutants.

Results

Discovery of M^{pro}/TMPRSS2 bispecific inhibitor with highly potent anti-coronavirus efficacy in vitro

To obtain a compound candidate with bispecific inhibition potential, we first established fluorescence resonance energy transfer (FRET)-based enzymatic assays with recombinant SARS-CoV-2 Omicron main protease (M^{pro}) and the enzymatically-active TMPRSS2 ectodomain, as we and others previously established[34,36]. We then screened an in-house de novo synthesized chemical library consisting of over 5000 small-molecule or peptidomimetic candidates as we previously reported[32,34]. The peptidomimetic candidates in our library ranged from dipeptidyl to tetrapeptidyl derivatives that mimicked the natural peptide substrate of M^{pro}, while the small-molecule inhibitors have been optimized to improve drug-like properties. Primary screening resulted in a lead compound **E87** with both anti-M^{pro} and TMPRSS2 activity, exhibiting IC$_{50}$ values of 368.6 nM against M^{pro} and 15.21 μM against TMPRSS2. (Fig. 1a and Table 1). We next proceeded to optimize its potency against both M^{pro} and TMPRSS2. The structural optimization was focused on Region-I to Region-IV on **E87** (Fig. 1a), and a stepwise optimization strategy was applied.

In the first step, we optimized Region-I with Region-II, III, and IV fixed as in **E87**. Eight compounds (**10a–h**) with different fragments at Region-I were designed and synthesized. Bioactivities of these compounds are displayed in Table 1. Compound **10a** with the same fragment at Region-I (R^1) as that of **E87** but with a different configuration (R-configuration) showed decreased activity against both M^{pro} and TMPRSS2, indicating the S-configuration was preferred at R^1. We thus prepared a series of compounds (**10b–g**) containing different substituents with S-configuration at R^1. Compared with **E87**, compounds **10c–d** and **10f–h** showed increased activity against M^{pro}, but only **10g** exhibited increased activity against TMPRSS2. The R^1 substituent in **10g**, (S)-2-cyclohexyl, was thus set as an optimal fragment in the following optimization.

In the second step, we optimized Region-II with Region-III, IV fixed as original subgroups, and Region-I as the optimal (S)-2-cyclohexyl. Eight compounds (**13a–h**) were designed and synthesized. Bioactivities of compounds **13a–h** are displayed in Table 2. All of the tested compounds showed significantly decreased activity against TMPRSS2 (>30 μM), although some of them displayed increased activity against M^{pro}. Therefore, Region II remained unchanged as that in **E87**.

In the third step, we optimized Region-III with Region-I and II as their optimal substituents and Region-IV as in **E87**. Ten compounds (**18a–j**) were designed and synthesized. Bioactivities of compounds **18a–j** are displayed in Table 3. Compound **18a** generated by replacing (1S,3aR,6aS)-octahydrocyclopenta[c]pyrrole-1-formamide group with phenylalanine exhibited improved M^{pro} inhibitory activity with an IC$_{50}$ value of 19.1 nM, while it completely lost activity against TMPRSS2, suggesting Region III specifically affects the inhibition against TMPRSS2. To explore the optimal inhibition against TMPRSS2, we prepared **18b–j**, containing different dicyclic or monocyclic groups in Region III. **18c–d** and **18f** showed increased activity against M^{pro}, but decreased activity against TMPRSS2. Compounds **18e** and **18g–j** displayed increased activity against TMPRSS2, but decreased activity against M^{pro}. To balance the inhibition against TMPRSS2 and M^{pro}, we prioritized **18e** as the optimal compound in this step.

Finally, we optimized Region-IV with other regions fixed as their optimal fragments. We designed and synthesized four compounds (**24a–d**). Bioactivities of these compounds are displayed in Table 4. All four compounds showed comparable potency against M^{pro} as **18e** but only **24d (TMP1)** displayed increased activity against TMPRSS2. Overall, through the above structural optimization and structure-activity relationship (SAR) studies, we obtained a series of α-ketoamide-containing dual inhibitors against M^{pro} and TMPRSS2. Among them, compound **TMP1** is the most potent one with an IC$_{50}$ value of 1.28 μM against TMPRSS2 and 312.5 nM against M^{pro}.

Next, we comprehensively characterized the antiviral potency of TMP1 against wildtype SARS-CoV-2 and other variants of concern (VOCs) including Alpha, Beta, Delta, and Omicron (BA.1 and JN.1) in VeroE6-TMPRSS2 cells. To exclude cellular cytotoxicity caused by TMP1 treatment, we performed in vitro cytotoxicity assays. Our results indicated no significant in vitro cytotoxicity was found at the therapeutic concentrations used in this study (Supplementary Fig. 1). Because VeroE6, VeroE6-TMPRSS2, and LLC-MK2 cells express high levels of the efflux transporter P-glycoprotein (P-gp)[33,37], for which TMP1 is a substrate (Supplementary Fig. 2), our in vitro antiviral assays with VeroE6, VeroE6-TMPRSS2, and LLC-MK2 cells were conducted in the presence of 2 μM P-gp inhibitor CP-100356. Our results showed that TMP1 potently reduced both viral burden and infectious progeny viral titres in a dose-dependent manner in vitro (Fig. 1b and c). Plaque assays demonstrated comparable EC$_{50}$ of TMP1 against wildtype SARS-CoV-2 and the tested VOCs, which varied between 0.73 to 3.76 μM (Fig. 1c). M^{pro} is structurally and functionally conserved in the *Coronaviradae* family[29]. Given TMPRSS2 is a key host protease and also functional receptor which are crucial for the entry of not only SARS-CoV-2 but also other HCoVs[10,11,20,38], we extended our investigations to examine the antiviral efficacy of TMP1 against all remaining six pathogenic HCoVs which caused outbreaks or endemics in history. We found that TMP1 potently inhibited the replication of seasonal HCoVs

(HCoV-HKU1, -OC43, -NL63 and -229E) with EC_{50} ranging from 0.31 to 2.60 μM (Fig. 1d and e). Moreover, TMP1 cross-protected against highly-pathogenic coronaviruses SARS-CoV-1 and MERS-CoV in a dose-dependent manner (Supplementary Fig. 3 and Supplementary Table 1) with the EC_{50} of 0.55 and 5.26 μM (Fig. 1e). Collectively, our in vitro data demonstrates the M^{pro}/TMPRSS2 bispecific inhibitor TMP1 not only suppresses the infection of SARS-CoV-2 but also potently protects against all other human-pathogenic coronaviruses.

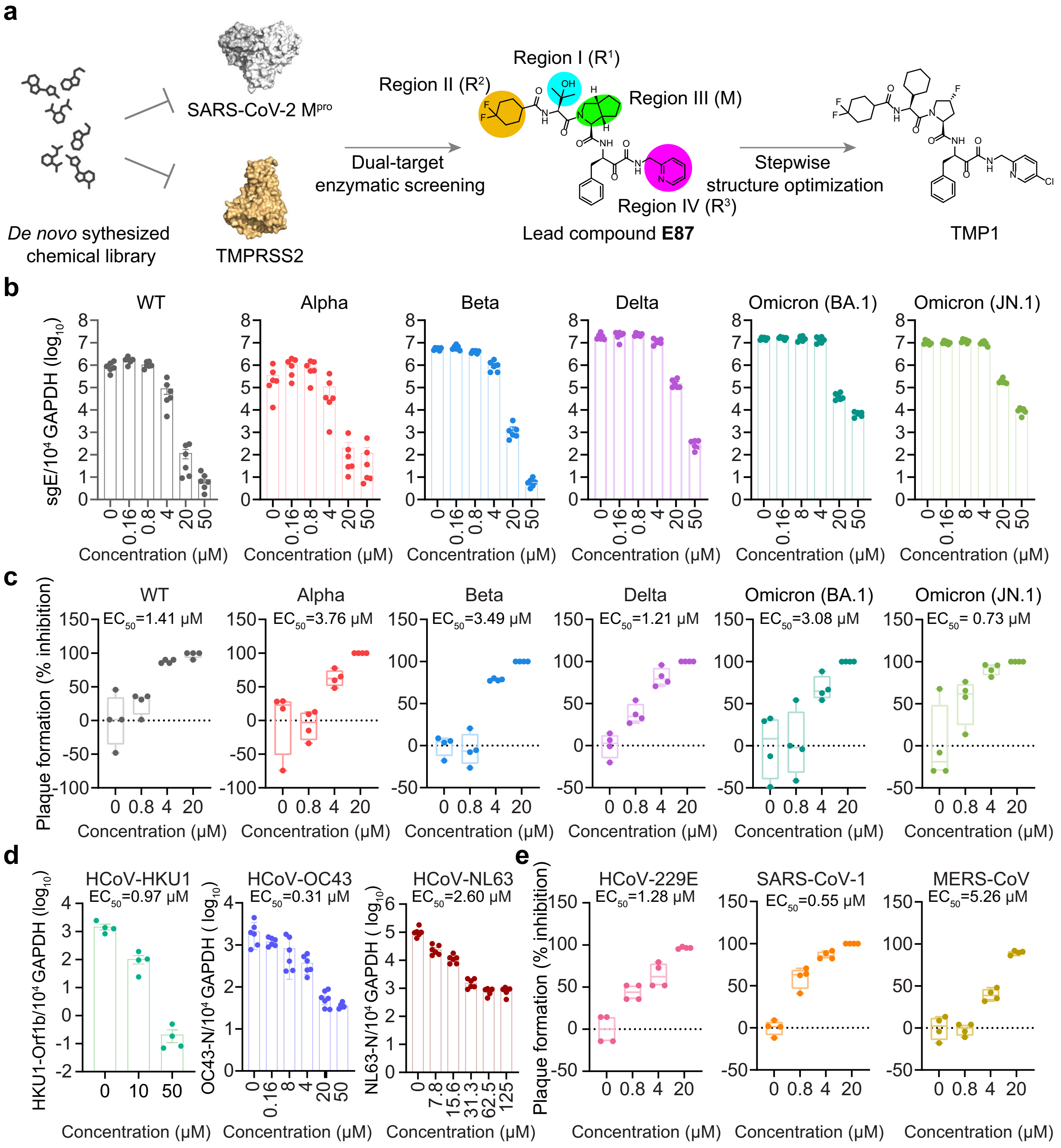

Fig. 1 | Discovery of the M^{pro}/TMPRSS2 bispecific inhibitor with highly potent anti-coronavirus efficacy. a Schematic illustration of the screening workflow for the discovery of M^{pro}/TMPRSS2 bispecific inhibitor. **b** Quantification of the subgenomic envelope (sgE) gene in VeroE6-TMPRSS2 cells ($n = 6$) infected with wildtype SARS-CoV-2 and Alpha, Beta, Delta, Omicron (BA.1 and JN.1) variants in the presence or absence of TMP1. Lysates were harvested at 24 hours post infection (hpi). for one-step reverse transcription and quantitative polymerase chain reaction (RT-qPCR) analysis. **c** Infectious viral titres in the supernatants harvested at 24 hpi. from VeroE6-TMPRSS2 cells ($n = 4$) infected with wildtype SARS-CoV-2 and Alpha, Beta, Delta, Omicron (BA.1 and JN.1) variants were determined by plaque assays. Number of plaques were normalized to those recovered from supernatants with mock treatment only. **d** Quantification of the viral Orf1b and N gene with RT-qPCR in primary human nasal epithelial cells (hNECs) ($n = 4$), MRC-5 ($n = 6$) and LLC-MK2 ($n = 6$) cells infected with HCoV-HKU1, -OC43 and -NL63 at 48 hpi. **e** Infectious viral titres in the supernatants harvested at 24 hpi from Huh7 infected with HCoV-229E or VeroE6-TMPRSS2 cells ($n = 4$) infected with SARS-CoV-1 and MERS-CoV were determined in Huh7 cells (for HCoV-229E) or VeroE6-TMPRSS2 (for SARS-CoV-1 and MERS-CoV) by plaque assays. Each data point represents one biological repeat. Data represent mean ± SEM from the indicated number of biological repeats. For box-and-whisker plot shown, whiskers bounded the min-max values of the data, the bounds of the box represented lower (Q1)/upper (Q3) quartiles, and the central value represented the median value. Data were obtained from three independent experiments. WT, wildtype SARS-CoV-2.

Table 1 | Chemical structures and bioactivities of compounds 10a–h

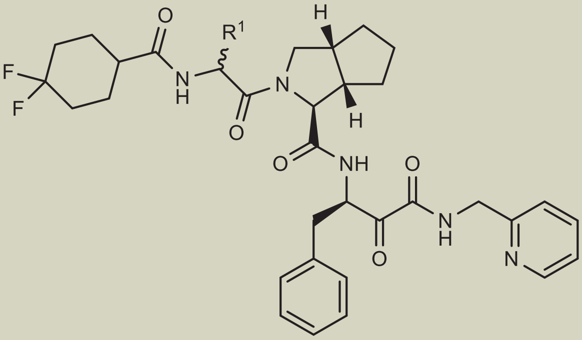

Chemical modifications in R^1

Compound	R^1	M^{pro} (nM)	TMPRSS2 (μM)
E87		368.6 ± 5.0	15.21 ± 5.90
10a		596.8 ± 1.5	223.98 ± 20.16
10b	H	528.8 ± 8.3	>500
10c		85.3 ± 1.2	38.04 ± 8.92
10 d		175.5 ± 3.5	96.24 ± 16.38
10e	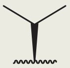	556.4 ± 1.3	49.28 ± 3.73
10f		66.5 ± 1.0	45.51 ± 4.59
10g	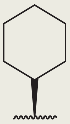	82.7 ± 1.7	11.22 ± 0.96
10h	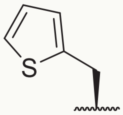	301.6 ± 1.4	27.73 ± 1.48

Bispecific inhibitor TMP1 demonstrates potent antiviral efficacy in vivo and rescues hACE2 transgenic mice from lethal SARS-CoV-2 infection

Oral bioavailability of antiviral treatment is critical to its timely application during emerging pandemics. Therefore, we characterized the oral pharmacokinetics (PK) of TMP1 in mice before in vivo antiviral efficacy evaluation. Our data suggested that ritonavir (RTV) significantly increase the plasma concentration of TMP1 (Supplementary Fig. 4a). Therefore, RTV was included as pharmacokinetic enhancer for all treatment groups. We further found that upon single-dose oral administration, plasma concentration of absorbed TMP1 maintained above the EC_{50} against SARS-CoV-2 M^{pro} and TMPRSS2 for over 16 and 12 hours, respectively (Fig. 2a). The maximum blood concentration (C_{max}) of 8028.86 μg/L (equivalent to 11.2 μM) was reached at 3.33 h post-delivery, resulting in an oral availability of 77.5% in mice (Table 5). To evaluate the redistribution of TMP1 in different organ tissues after absorption into the plasma, we measured the TMP1 concentration in lung, brain, liver, kidney and intestine tissues of the treated mice. Our results indicated that TMP1 could be maintained at 11.1-, 11.4- and 6.5-fold higher than its in vitro EC_{50} of SARS-CoV-2 Delta at 1, 2 and 8 hours post oral delivery (Supplementary Fig. 4b and c). To exclude in vivo toxicity caused by TMP1, mice were given 150 mg/kg/dose, twice per day of TMP1 for a consecutive of 4 days. Body weight, kidney and liver function and tissue sections for histopathological analysis of the treated mice were monitored and we found no signs of in vivo toxicity at the given dosage and dosing frequency (Supplementary Fig. 5). In parallel, we examined the oral bioavailability of Paxlovid and camostat mesylate, which are clinically-approved M^{pro} and TMPRSS2 inhibitors for COVID-19 treatment[33,39] (Fig. 2a). Consistent with previous results from the literature, plasma concentration of Paxlovid quickly reached over 10000 μg/L (equivalent to 20 μM) upon oral delivery[33]. To our surprise, although mice were treated with an oral dosage equivalent to

Table 2 | Chemical structures and bioactivities of compounds 10g and 13a-h

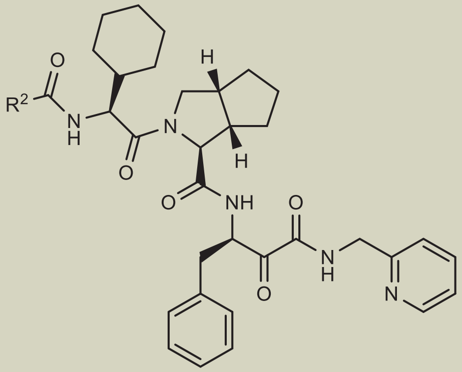

Chemical modifications in R^2

Compound	R^2	M^{pro} (nM)	TMPRSS2 (µM)
10g	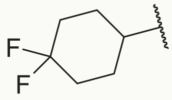	82.7 ± 1.7	11.22 ± 0.96
13a	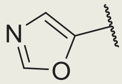	37.9 ± 1.3	32.66 ± 1.23
13b	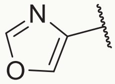	42.8 ± 1.6	50.13 ± 2.79
13c	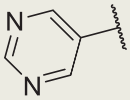	120.4 ± 1.1	52.97 ± 0.02
13d	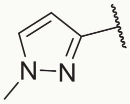	38.8 ± 1.4	52.66 ± 4.81
13e	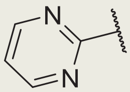	19.2 ± 0.9	167.00 ± 1.93
13f	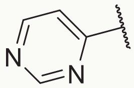	27.3 ± 1.2	238.88 ± 7.63
13g	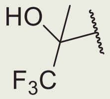	105.3 ± 4.0	>500
13h		61.3 ± 0.5	431.82 ± 0.12

that was used in COVID-19 patients[39,40], no detectable level of camostat mesylate, but only its metabolite, 4-(4-guanidinobenzoyloxy) phenylacetic acid (GBPA), was found in the plasma after oral delivery. However, plasma concentration of GBPA remained below its EC_{50} against TMPRSS2 (Fig. 2a and Supplementary Fig. 6). Our data suggested that despite its strong anti-TMPRSS2 potency in vitro, oral delivery of camostat mesylate might not be an optimal therapeutic option for SARS-CoV-2 treatment in vivo. Consequently, we selected Paxlovid monotherapy over combined camostat mesylate and Paxlovid treatment for side-by-side comparison with TMP1 in subsequent in vivo assays.

We next proceeded to investigate the in vivo antiviral potency of TMP1 using the K18 human ACE2 (K18-hACE2) transgenic mice, which is a well-established infection model for COVID-19 research[41–43]. Briefly, mice were orally treated twice per day with vehicle only, TMP1 or Paxlovid. Prophylactic treatment began at 1 day prior to challenge with SARS-CoV-2 Delta variant and lasted until day 2 post virus challenge (Fig. 2b). Viral genome quantification and infectious viral progenies titration at 3 days post infection (dpi.) showed that TMP1 significantly suppressed SARS-CoV-2 infection to a comparable level as Paxlovid in the nasal turbinates (Fig. 2c and d). Notably, viral burdens in the lung tissues were reduced to even lower levels in the TMP1-treated mice when compared with those treated with Paxlovid (reduction in lung viral gene copies: [TMP1 vs Paxlovid]: 151.2-fold vs 27.1-fold); reduction in lung infectious viral titres: [TMP1 vs Paxlovid]: 46.0-fold vs 37.4-fold) (Fig. 2c and d), though the differences have not yet reached statistical significance.

To examine viral antigen expression in vivo, we detected the coronavirus nucleocapsid (N) protein by immunohistochemistry (IHC) staining using specific anti-sarbecovirus N antibodies. Abundant amount of viral N protein was found in both nasal turbinate and

Table 3 | Chemical structures and bioactivities of compounds 10g and 18a–j

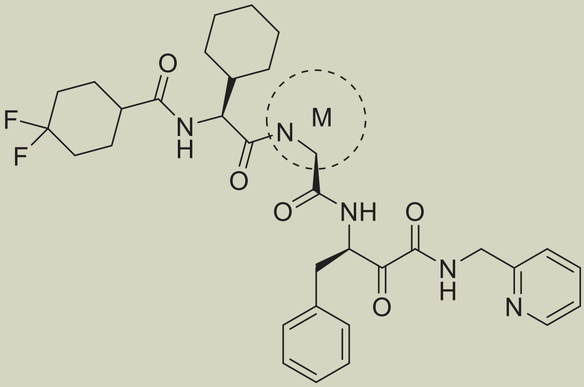

Chemical modifications in M

Compound	M	M^{pro} (nM)	TMPRSS2 (μM)
10g	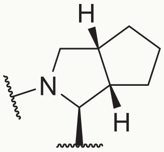	82.7 ± 1.7	11.22 ± 0.96
18a	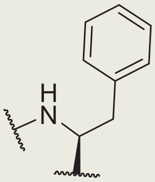	19.1 ± 0.3	>500
18b	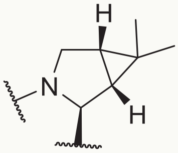	148.9 ± 2.4	30.53 ± 7.81
18c	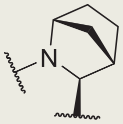	48.2 ± 4.0	40.81 ± 0.05
18d	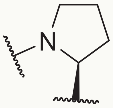	34.2 ± 1.2	38.39 ± 0.69
18e	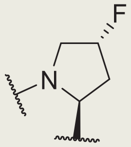	233.3 ± 2.2	3.42 ± 0.08
18f	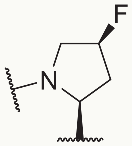	47.3 ± 0.5	15.09 ± 0.16
18g	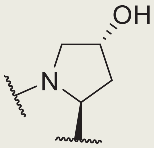	104.1 ± 2.0	6.22 ± 1.45

Table 3 (continued) | Chemical structures and bioactivities of compounds 10g and 18a–j

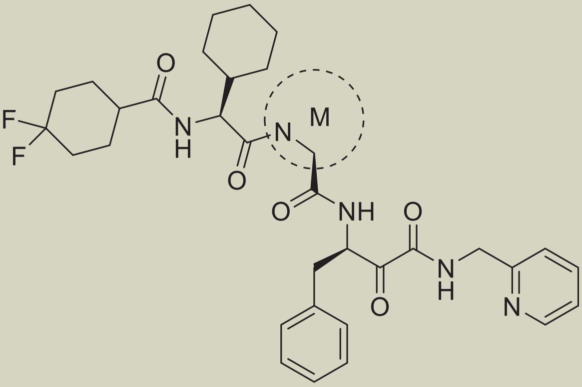

Chemical modifications in M

Compound	M	M^{pro} (nM)	TMPRSS2 (μM)
18h	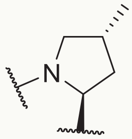	204.8 ± 2.5	10.73 ± 0.17
18i	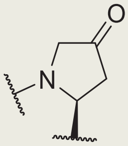	1040 ± 100	3.06 ± 1.02
18j	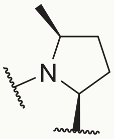	240.9 ± 7.5	5.03 ± 0.28

lung tissues of vehicle-treated mice (Fig. 2e and f). In comparison, expression of N protein was significantly lowered by TMP1 treatment, which was further verified with quantification of the viral antigen positive area (Fig. 2e and f). Additionally, H&E staining was performed to identify infection-related histopathological lesions in the nasal turbinate and lung tissues. In line with the earlier virological findings, signs of virus-induced pathologies, including loss of epithelium integrity, septal inflammation, alveoli deformation, and submucosal inflammatory infiltrations were found most evident in the vehicle-treated mice. On the contrary, these histopathological changes were largely alleviated or absent in their TMP1-treated counterparts (Fig. 2g).

Next, we sought to answer whether TMP1 treatment might rescue animals from lethal SARS-CoV-2 challenge. We infected the transgenic mice with lethal dose (1250 PFU per mouse) of SARS-CoV-2 Delta and monitored animal survival for 14 days. Vehicle-treated mice developed continuous body weight loss and began to succumb to lethal virus challenge as early as 6 dpi., resulting in 16.7% survival for the female mice and 0% for the male mice at 14 dpi. (Fig. 2h and i). In contrast, TMP1-treated mice were observed with delayed onset of death (Vehicle: 6 dpi. vs TMP1: 9 dpi.). The survival rate was significantly rescued to 83.3% ($P = 0.0049$) and 69.2% ($P = 0.0098$) for female and male mice, respectively (Fig. 2h and i). To explore the therapeutic potential of TMP1, we initiated the antiviral treatment at a delayed timepoint at 24 hpi. We found that TMP1 still significantly lowered viral gene copies by 7.3- ($P < 0.0001$) and 9.2-fold ($P < 0.0001$) in the nasal turbinate and lung tissues, respectively (Fig. 2j). Together, our in vivo data suggests that prophylactic and therapeutic TMP1 treatments robustly reduce viral burdens in the infected mouse airways and ameliorate infection-associated tissue pathology, thus improving the overall survival of the infected animals.

Bispecific inhibitor TMP1 substantially reduces SARS-CoV-2 infection in human airway epithelium and blocks SARS-CoV-2 transmission in golden Syrian hamsters

TMPRSS2 expression in the airway epithelium is a key determinant of coronavirus transmission in vivo[24]. We next asked whether the improved bispecific design to include TMPRSS2 as one of the antiviral targets might help to block coronavirus transmission. To evaluate this question, we first infected the air-liquid interface-cultured human nasal epithelial cells (ALI-hNECs) with two SARS-CoV-2 Omicron prevalent subvariants JN.1 and KP.2 to mimic coronavirus infection at the primary infection site (Fig. 3a). Our results indicated that TMP1 treatment significantly decreased the viral gene copies by approximately one log and the infectious viral titres by more than one log for both subvariants in the infected ALI-hNECs (Fig. 3b and c), demonstrating the potential of TMP1 in suppressing SARS-CoV-2 infection in the human upper airways.

Next, we evaluated the impact of TMP1 treatment on SARS-CoV-2 transmission using the golden Syrian hamster transmission model as we and others previously established[44,45]. To better simulate the scenario in the human population, only the index but not the contact hamsters were treated. Briefly, index hamsters with or without TMP1 oral treatment were intranasally inoculated with 2000 PFU SARS-CoV-2 Delta and rested overnight. On the next day, the infected index hamsters were co-housed with naïve contacts for five hours to allow virus transmission. Contacts were then separated and individually housed for three more days until tissue harvest at 4 dpi. (Fig. 3d).

Table 4 | Chemical structures and bioactivities of compounds 18e and 24a–d

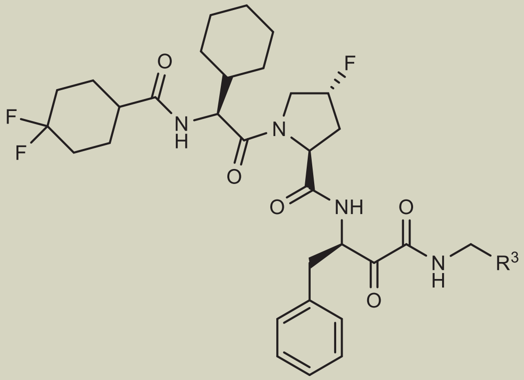

Chemical modifications in R^3

Compound	R^3	M^{pro} (nM)	TMPRSS2 (μM)
18e	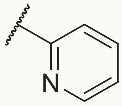	233.3 ± 2.2	3.42 ± 0.08
24a	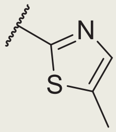	159.2 ± 1.9	18.70 ± 3.63
24b	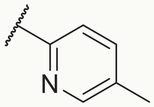	155.7 ± 1.0	3.69 ± 0.81
24c	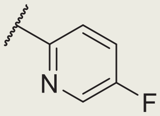	69.4 ± 0.8	61.03 ± 3.02
24d (TMP1)	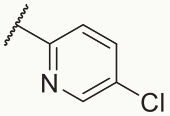	312.5 ± 5.7	1.28 ± 0.43

Compared with contact hamsters in the control group, those in contact with the TMP1-treated hamsters experienced 29.1-fold ($P = 0.0382$) and 154.4-fold ($P = 0.0383$) lower viral gene copies and infectious viral titres in the nasal turbinates, respectively (Fig. 3e and f). Similarly, viral burdens in the lung tissues of contact hamsters of the TMP1 treatment group were remarkably lower (viral gene copies: 29.5-fold reduction, $P = 0.0409$; infectious viral titres: 58.1-fold reduction, $P = 0.0177$) than their control group littermates (Fig. 3e and f). Importantly, infectious progeny viruses were not recovered from two contact hamster lungs out of the six samples (33.3 % protection) in the TMP1 contact group (Fig. 3f). In corroboration with viral burdens quantification, viral N protein expression was scarcely detected in the nasal turbinates or lungs of the TMP1 contact hamsters with IHC staining, which was dramatically different from the abundant viral N protein expression in the control contact hamsters (Fig. 3g and h). Histopathological analysis revealed that while extensive loss of integrity in the nasal epithelium and large amounts of necrotic cell debris in the nasal cavity was found in the control contact hamsters, only dispersed epithelial cell loss was occasionally detected in the TMP1 group (Fig. 3i). Consistently, while massive inflammatory infiltrations in alveolar septa and alveoli deformation were present in the control contact hamster lungs, these pathological findings were largely absent in the TMP1 contact hamsters (Fig. 3i). Together, our results demonstrate that our bispecific inhibitor TMP1 is effective against the prevalent Omicron lineage in the human upper airway epithelium and effectively attenuates SARS-CoV-2 transmission in vivo.

Bispecific inhibitor TMP1 cross-protects against highly-pathogenic human coronaviruses in vivo

Inspired by the strong in vivo antiviral potency of TMP1 against SARS-CoV-2, we were interested in exploring the cross-protection of TMP1 against other highly-pathogenic human coronaviruses in vivo. To this end, we first examined the antiviral potency of TMP1 against SARS-CoV-1, which is also a human-pathogenic sarbecovirus that utilized ACE2 as entry receptor (Fig. 4a). Our results demonstrated that TMP1-treated SARS-CoV-1-infected K18-hACE2 transgenic mice experienced significantly lower viral burdens in both nasal turbinate and lung tissues when compared with that of the control mice (Fig. 4b). In particular, titres of infectious viral progenies were reduced by 29.9-fold in the TMP1-treated mouse lungs (Fig. 4c). Strikingly, four out of eight TMP1-treated transgenic mice developed no detectable level of infectious viral titres in the lungs, suggesting TMP1 treatment led to sterile protection in 50% of the challenged animals. In parallel, IHC staining also verified the viral load quantification and revealed that SARS-CoV-1 nucleocapsid protein expression was significantly reduced by 5.4-fold ($P = 0.0191$) and 5.7-fold ($P = 0.0236$) by TMP1 treatment in

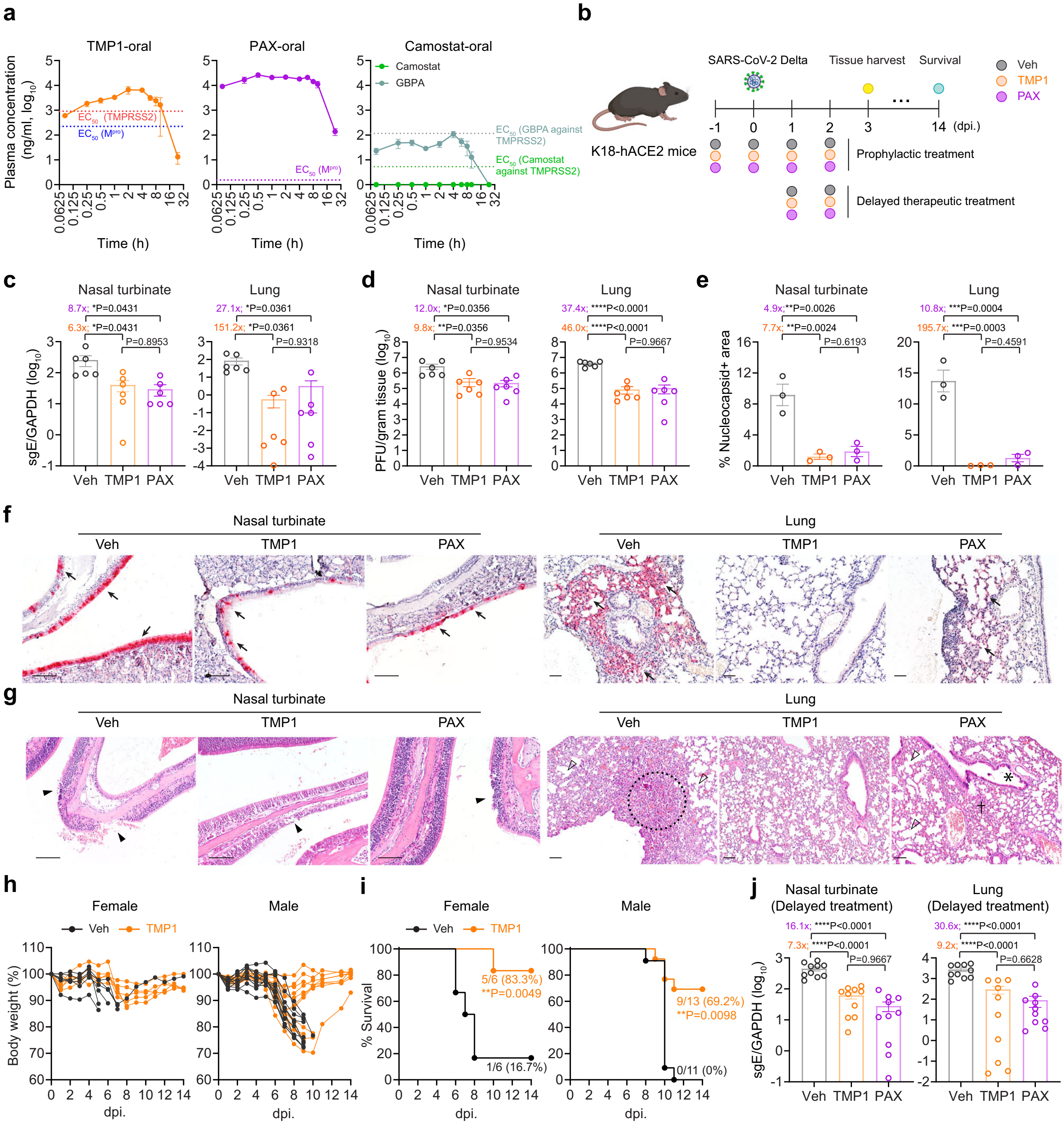

Fig. 2 | The in vivo antiviral efficacy of prophylactic and therapeutic TMP1 treatment against SARS-CoV-2 infection. a Pharmacokinetics of TMP1, Paxlovid and camostat oral delivery in mice ($n = 3$). **b** Schematic illustration of SARS-CoV-2 infection in K18-hACE2 transgenic mice with therapeutic or prophylactic TMP1 treatment (Created in BioRender)[104]. **c** Quantification of sgE gene of SARS-CoV-2 in the nasal turbinate and lung tissues of the infected mice ($n = 6$) with prophylactic treatment. **d** Quantification of the infectious viral titres in the nasal turbinate and lung tissues of the infected mice ($n = 6$) with prophylactic treatment. **e** Viral N protein expression in the nasal turbinate and lung tissues of infected mice ($n = 3$) with prophylactic treatment was quantified with ImageJ. **f** Representative images of SARS-CoV-2 N protein expression (black arrow) in nasal turbinate and lung tissue of the infected mice. Scale bar represents 100 μm. **g** Histology analysis of the nasal turbinate and lung tissue of the infected mice by H&E staining. Scale bar represents 100 μm. Black arrowhead, nasal epithelial desquamation; open arrowhead, alveolar collapse; dashed circle, inflammation infiltrations in alveolar septa; asterisk, bronchiolar epithelium damage. **h** Body weight change of the female ($n = 6$) and male ($n = 11$ and 13 for vehicle and TMP1 group, respectively) infected mice with or without TMP1 prophylactic treatment. **i** Survival of the female ($n = 6$) and male ($n = 11$ and 13 for vehicle and TMP1 group, respectively) infected mice with or without TMP1 prophylactic treatment. **j** Quantification of sgE gene of SARS-CoV-2 in the nasal turbinate and lung tissues of the infected mice ($n = 10$) with delayed therapeutic treatment. Each data point represents one biological repeat. Data represents mean ± SEM from the indicated number of biological repeats. Statistical significances were determined using one way-ANOVA with Dunnett's multiple comparisons test (**c**–**e**), (**j**) and log-rank (Mantel-Cox) tests (**i**). Data were obtained from three independent experiments. * represented $p < 0.05$ and ** represented $p < 0.01$. *** represented $p < 0.001$, **** represented $p < 0.0001$. WT wildtype SARS-CoV-2, Veh vehicle, PAX Paxlovid.

Table 5 | Pharmacokinetics of oral delivery of TMP1 in BALB/c mice

Compd.	Animal	Admin.	$T_{1/2}$ (h)	T_{max} (h)	C_{max} (μg/L)	$AUC_{(0\sim t)}$ (μg/L*h)	$AUC_{(0\sim\infty)}$ (μg/L*h)	$MTR_{(0\sim t)}$ (h)	CLz (L/h/kg)	Vz (L/kg)	F %
TMP1	BALB/c mice	i.v. (0.5 mg/kg)	0.56 ± 0.21	0.08 ± 0.01	785.37 ± 117.02	329.61 ± 51.56	329.90 ± 51.79	0.43 ± 0.11	1.54 ± 0.24	1.20 ± 0.32	-
		p.o. (100 mg/kg)*	2.22 ± 0.37	3.33 ± 1.16	8028.86 ± 2542.35	51072.79 ± 31482.58	51118.64 ± 31475.82	4.91 ± 1.63	-	-	77.47 ± 47.76

Data are shown as mean ± SD, $n = 3$.

*Mice were orally treated with 100 mg/kg TMP1 in combination with 20 mg/kg ritonavir.

nasal turbinate and lung tissues, respectively (Fig. 4d and e). Concordantly, while histopathological findings including loss of epithelium integrity in the nasal mucosa and alveoli damage were evident in the control mice (Fig. 4f), the epithelial lining remained largely intact in the nasal turbinate of the TMP1-treated mice and only mild inflammatory infiltrations were discernible in the alveolar septa in the lungs (Fig. 4f).

To further extend our findings to other human-pathogenic coronaviruses that are more evolutionarily distant, we challenged human dipeptidyl peptidase 4 knock-in mice (hDPP4-KI mice) with a lethal dose (5000 PFU) of mouse-adapted MERS-CoV (MERS-CoV_{MA}) with or without TMP1 oral treatment and harvested nasal turbinate and lung samples on 3 dpi. for virological assessments (Fig. 4g). In keeping with our earlier findings with SARS-CoV-1, TMP1 treatment suppressed MERS-CoV_{MA} replication in both nasal turbinates and lungs when compared with control mice (Fig. 4h). Infectious viral titres were decreased by 4.6- ($P = 0.0219$) and 8.1-fold ($P = 0.0044$) in the nasal turbinate and lung tissues, respectively (Fig. 4i). Consistent with the viral burden findings, expression of MERS-CoV_{MA} N protein was reduced in TMP1-treated mouse nasal turbinate and lung tissues (Supplementary Fig. 7a). Additionally, histological analysis indicated TMP1 treatment alleviated virus-induced epithelial damage in the nasal turbinate and reduced alveolar destruction in the infected mice (Supplementary Fig. 7b). Together, these in vivo findings with SARS-CoV-1 and MERS-CoV_{MA} infection corroboratively supports our hypothesis that oral administration of the M^{pro}/TMPRSS2 bispecific inhibitor confers broad-spectrum antiviral protection against highly-pathogenic coronaviruses.

Bispecific inhibitor TMP1 binds to TMPRSS2 enzymatic pocket to suppress TMPRSS2-dependent coronavirus entry

To mechanistically demonstrate that TMP1 indeed possesses specific inhibition against the targeted host protease TMPRSS2, we set out to characterize its binding with TMPRSS2 by surface plasmon resonance (SPR) analysis. The SPR analysis revealed direct interaction between TMP1 and TMPRSS2 with a K_D value of 10.10×10^{-6} M (Fig. 5a). FRET-based enzymatic assay further confirmed TMP1 inhibited the protease activity of recombinant TMPRSS2 at an IC_{50} of 1.28 μM (Fig. 5b). As a positive control, we also measured the efficacy of camonstat using the TMPRSS2 enzymatic assay. IC_{50} of camostat against TMPRSS2 resulted in 10.5 ± 0.9 nM (Supplementary Fig. 6b), which was in accordance with previous literature[9]. TMPRSS2 cleaves the spike proteins at S2′, exposing the fusion peptide to facilitate virus entry[46].

To study the anti-TMPRSS2 potency of TMP1 independent of its anti-M^{pro} activity, we first investigated whether TMP1 might reduce TMPRSS2-mediated coronavirus entry. To this end, we pre-treated VeroE6-TMPRSS2 with TMP1 followed by infection of SARS-CoV-2 spike-pseudoviruses. Measurement of luciferase signals indicated that TMP1 dose-dependently reduced SARS-CoV-2 pseudovirus entry (Fig. 5c). Similarly, TMP1 prevented the entry of HCoV-229E, SARS-CoV-1, and MERS-CoV pseudoviruses, showing a broad spectrum of inhibition on TMPRSS2-dependent coronavirus entry (Fig. 5c). Additionally, we performed the split-GFP assay that found TMP1 efficiently suppressed TMPRSS2-dependent cell-cell fusion mediated by SARS-CoV-2 wildtype spike in side-by-side comparison with camostat mesylate (Fig. 5d and e). To exclude the possibility of off-target inhibition against other host proteases, we cross-examined the potential inhibition of TMP1 against a panel of other host proteases, including calpain1, cathepsin L/D and thrombin (Table 6). Our data indicated that TMP1 was highly selective against TMPRSS2 over the other human cysteine/serine proteases.

To illustrate the binding mode of TMP1 with TMPRSS2, we tried to solve the co-crystal structure of TMPRSS2 in complex with TMP1 but it was unsuccessful. Alternatively, we performed molecular docking to predict possible interactions between TMP1 and TMPRSS2, followed

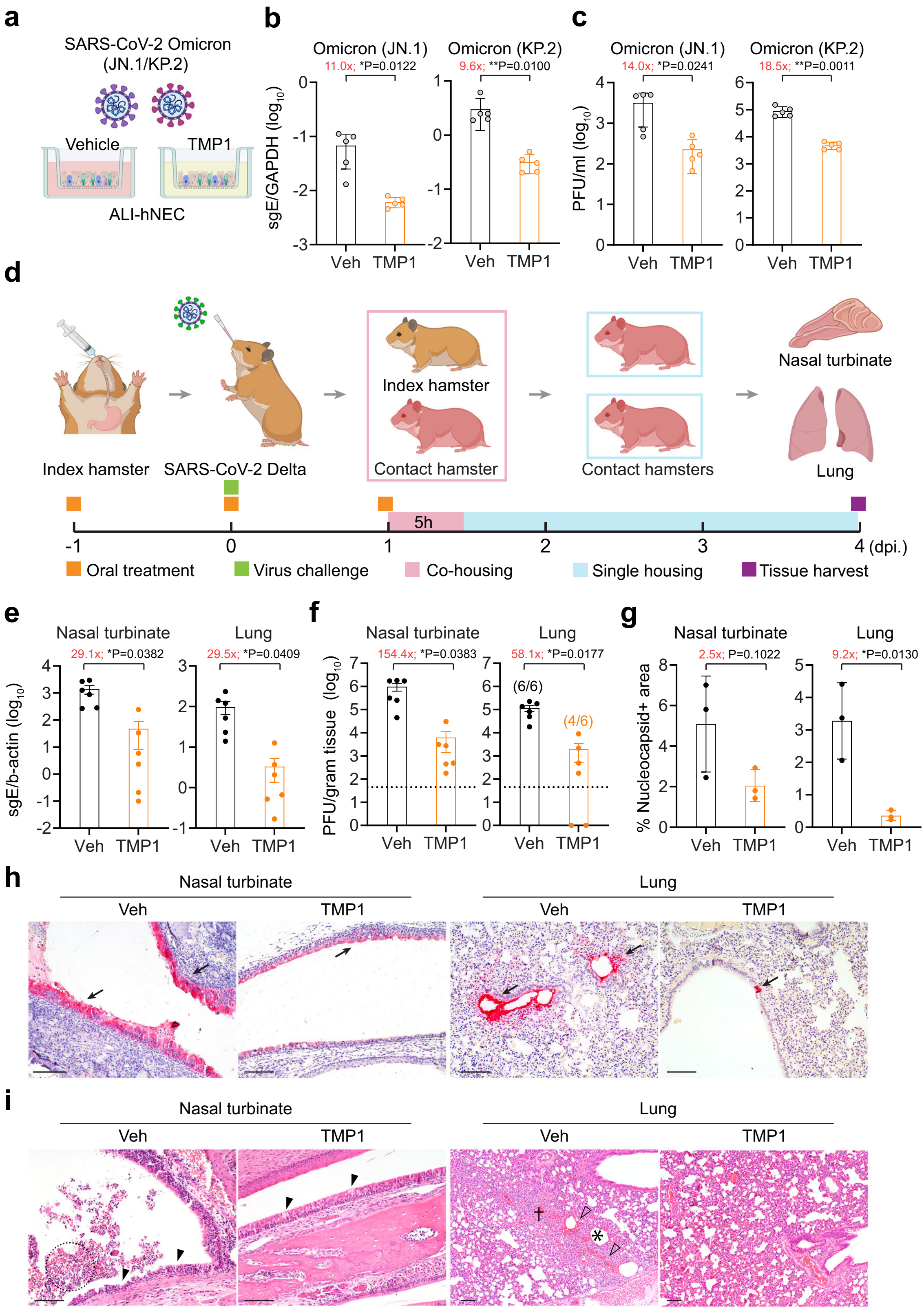

by verification with mutagenesis assays. As shown by the molecular docking analysis, TMP1 resided in a large hydrophobic pocket of TMPRSS2, which contained a catalytic site formed by the catalytic triad of H296, D345, and S441 (Fig. 5f). It formed strong hydrophobic interactions with P301, L302, V280, K390, H296, and C465. Additionally, TMP1 formed five hydrogen bonds (H-bonds) with residues Q438, G439, H296, and C297 (Fig. 5f).

To verify the interaction interface as predicted by our docking model, we mutated seven residues (V280, H296, P301, K390, Q438, L302, and T459) in TMPRSS2 that were predicted to be in close proximity with TMP1 (Fig. 5f). The distantly-located W461 was included as a negative control. Substitutions of Q438, L302, H296, and K390 to alanine resulted in a significant reduction in TMP1 potency by 312.5, 42.7, 24.2, and 6.8-fold, respectively (Fig. 5g and h), indicating

Fig. 3 | Efficacy of TMP1 in blocking SARS-CoV-2 transmission. a Schematic illustration of SARS-CoV-2 infection in human nasal epithelial cells (hNECs). Differentiated hNECs maintained in air-liquid interface (ALI) culture were infected with SARS-CoV-2 Omicron JN.1 or KP.2 with vehicle only or TMP1 treatment until sample harvest at 48 hpi (Created in BioRender[105]). **b** Quantification of SARS-CoV-2 sgE gene in the infected cell lysates ($n = 5$). **c** Quantification of the infectious viral titres in the apical supernatants ($n = 5$). **d** Schematic illustration of the SARS-CoV-2 transmission study in golden Syrian hamsters (Created in BioRender[106]). **e** Quantification of sgE gene of SARS-CoV-2 in the nasal turbinate and lung tissues of the contact hamsters ($n = 6$). **f** Quantification of the infectious viral titres in the nasal turbinate and lung tissues of the contact hamsters ($n = 6$). **g** Quantification of viral N protein expression in nasal turbinate and lung tissues of the contact hamsters ($n = 3$). Quantification was performed with ImageJ. **h** Representative images of SARS-CoV-2 N protein expression (black arrow) in nasal turbinate and lung tissue of the contact hamsters. Scale bar represents 100 μm. **i** Histology analysis of the nasal turbinate and lung tissue of the infected hamsters by H&E staining. Black arrowhead, nasal epithelial desquamation; dashed circle, necrotic cell debris in the nasal cavity; open arrowhead, hemorrhage in the alveolar septa; asterisk, alveoli collapse; cross, inflammatory infiltration in alveolar septa. Scale bar represents 100 μm. Each data point represents one biological repeat. Data represents mean ± SEM from the indicated number of biological repeats. Statistical significances were determined using two-tailed Student's *t*-test (**b**, **c**) and (**e**–**g**). Data were obtained from three independent experiments. * represented $p < 0.05$ and ** represented $p < 0.01$. Veh vehicle.

their crucial roles in TMP1 binding to TMPRSS2. Moreover, T459Y substitution, which introduced a larger side chain and causes steric hindrance (Supplementary Fig. 8) substantially reduced TMP1 potency by 9.8-fold (Fig. 5g and h). As expected, mutation W461A did not significantly affect the potency of TMP1 against TMPRSS2 (Fig. 5g and h). Together, these results strongly support that TMP1 might act through occupying the catalytic pocket of TMPRSS2 to inhibit its enzymatic activity and prevent TMPRSS2-mediated coronavirus entry.

To pinpoint the specific inhibition against TMPRSS2, we first performed protein sequence alignment with the TMPRSS2 from all animal species used in our current study, including human (*Homo sapiens*), African green monkey (*Chlorocebus sabaeus*), mouse (*Mus musculus*), hamster (*Mesocricetus auratus*) and rhesus macaque (*Macaca mulatta*). Alignment results indicated that the key amino acids responsible for the catalytic activity of TMPRSS2 are highly conserved among all these species (Supplementary Fig. 9a). We also performed molecular docking with TMP1 and the predicted structures of TMPRSS2 from the above species. We found the docking scores for African green monkey, mouse, hamster and rhesus macaque were 84.02, 76.20, 73.10, and 74.93, respectively (Supplementary Fig. 9b), which are comparable to that for humans (83.67).

Additionally, we synthesized a TMP1 analogue (Analogue-M^{pro}) which shared similar efficacy against SARS-CoV-2 M^{pro} as TMP1 but its efficacy against the TMPRSS2 was lost (Supplementary Fig. 10a and b). Our results showed that the EC_{50} of Analogue-M^{pro} against SARS-CoV-2 in Calu3 cells was 5.1-fold higher when compared to TMP1 (Supplementary Fig. 10c). Next, we synthesized another TMP1 analogue (Analogue-TMPRSS2) which preserved the anti-TMPRSS2 activity of TMP1 but with significantly attenuated anti-M^{pro} activity for in vitro treatment against SARS-CoV-2 (Supplementary Fig. 10d and e). We showed that intranasal treatment with Analogue-TMPRSS2 reduced viral gene copies by 1.9- and 2.4-fold in the nasal turbinate and lung tissues of the infected mice, respectively (Supplementary Fig. 10f). Collectively, our data demonstrates that the anti-TMPRSS2 activity of TMP1 is indispensable and acts together with its anti-M^{pro} activity to suppress SARS-CoV-2 infection.

Bispecific inhibitor TMP1 suppresses SARS-CoV-2 M^{pro} through covalent binding and inhibits nirmatrelvir-resistant SARS-CoV-2 infection in vivo

To better understand the mode of inhibition of TMP1 against M^{pro}, we determined the crystal structure of the M^{pro}-TMP1 complex at approximately 2.6 Å (PDB ID: 9IZB). The electron density map illustrated the binding mode of TMP1 with M^{pro} (Fig. 6a, **left panel**). The 5-chloropyridine at P1′ inserted into the S1 pocket, while the P1 benzyl group occupied S1′. The (R)-4-fluoropyrrolidine at P2 pointed towards the solvent region, and the (S)-2-cyclohexyl at P3, along with the 4,4-difluorocyclohexyl at P4, inserted into S2. The carbonyl carbon of TMP1's α-ketoamide warhead formed a reversible covalent bond (~1.8 Å) with C145's Sγ atom in the (R)-configuration (Fig. 6a**, right panel**). The hydroxy group of this thiohemiketal formed a hydrogen bond with H41 (~2.4 Å). The amide oxygen of TMP1 formed a hydrogen bond with G143 (~2.7 Å) and was oriented toward the "oxyanion hole" formed by the backbones of G143 and C145. The P1′ group formed hydrogen bonds with H163 (~3.2 Å) and H164 (~2.5 Å), and also engaged in hydrophobic interactions with F140, N142, M165, and E166. The P2 moiety was solvent-exposed, indicating flexibility for various functional groups. The P3 and P4 groups inserted into the hydrophobic S2 pocket, interacting with M49, D187, and Q189 (Fig. 6a**, right panel**). Simulation of TMP1 in complex with the M^{pro} of HCoV-229E, HCoV-NL63, HCoV-OC43, HCoV-HKU1, SARS-CoV-1, MERS-CoV, RaTG13 (bat-CoV) and GX/P3B (pangolin-CoV), supported the broad-spectrum inhibition potential of TMP1 against human-pathogenic coronaviruses and other mammalian sarbecoviruses (Fig. 6b and Supplementary Fig. 11). FRET-based enzymatic assay indicated a dose-dependent inhibition of TMP1 against recombinant SARS-CoV-2 M^{pro}, resulting in an IC_{50} of 0.313 μM (Fig. 6c). In parallel, we examined its efficacy against the M^{pro} of SARS-CoV-1 and MERS-CoV, resulting in the respective IC_{50} of 0.516 μM and 74.6 μM (Supplementary Fig. 12), which were in line with the in vivo efficacies of TMP1 against these highly pathogenic coronaviruses.

To study the antiviral potency of TMP1 independent of its anti-TMPRSS2 activity, we challenged the TMPRSS-2-deficient VeroE6 cells with wildtype SARS-CoV-2 and different VOCs. TMP1 treatment was started at the post-entry stage at 1 hour post infection (hpi.). Our data showed that the post-entry TMP1 treatment was still capable of reducing viral gene copies in SARS-CoV-2-infected VeroE6 cells (Fig. 6d and Supplementary Table 2), supporting that the bispecific inhibitor TMP1 indeed suppressed coronavirus replication by targeting coronavirus M^{pro}. In addition, we also investigated the possibility of broad-spectrum inhibition of TMP1 against the M^{pro} of other human-pathogenic coronaviruses. Our results suggested that TMP1 similarly decreased SARS-CoV-1 and MERS-CoV replication in VeroE6 cells in a dose-dependent manner (Fig. 6e), indicating that TMP1 not only inhibited the activity of SARS-CoV-2 M^{pro} but also that of the two highly-pathogenic coronaviruses.

Paxlovid has been most widely used as oral antiviral for COVID-19 treatment. Nevertheless, emerging nirmatrelvir (NRV)-resistant SARS-CoV-2 mutants has become a major public health concern[47–49]. Crystal structure data obtained in this study suggested the mode of interaction between TMP1 and M^{pro} were different from that of NRV (Fig. 6a and Supplementary Fig. 13). We further demonstrated with FRET assays that TMP1 was 16.8-fold less sensitive to NSP5-E166V mutation when compared with NRV (Fig. 6f), which is a dominant mutation leading to NRV-resistance found in COVID-19 patients[49,50]. The bispecific antiviral design is advantageous in combating drug-resistance caused by mono-target therapeutics. Therefore, we were interested to explore whether TMP1 might protect against the infection of NRV-resistant SARS-CoV-2 variants. To address this research question, we constructed recombinant SARS-CoV-2 (rSARS-CoV-2) that carried the NSP5-E166V mutation in the background of ancestral SARS-CoV-2 with

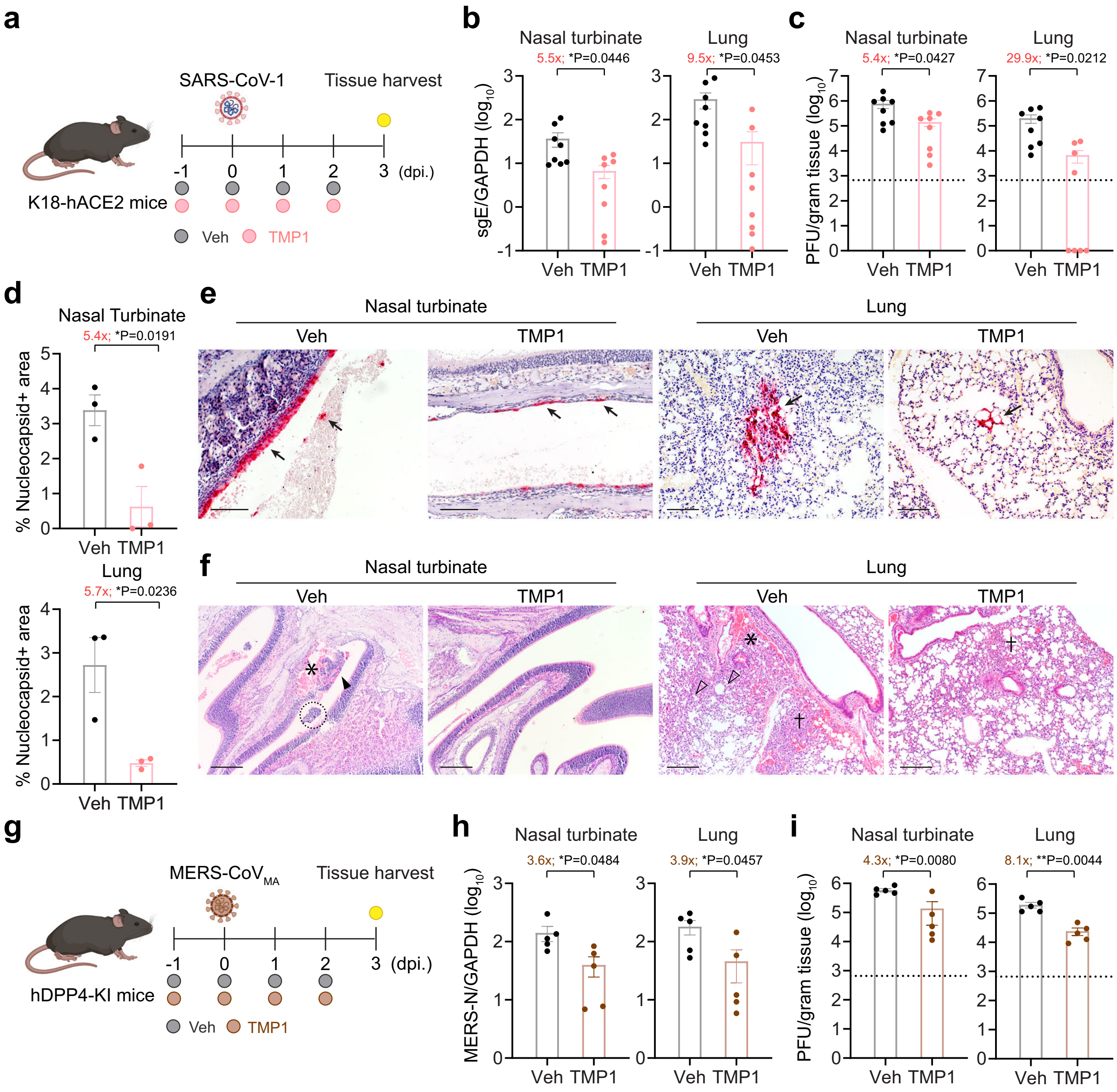

Fig. 4 | Cross-protection of TMP1 against highly-pathogenic human coronaviruses in vivo. a Schematic illustration of SARS-CoV-1 infection in K18-hACE2 transgenic mice with vehicle or TMP1 treatment (Created in BioRender)[107]. **b** Quantification of sgE gene of SARS-CoV-1 in the nasal turbinate and lung tissues of the infected mice with prophylactic treatment ($n = 8$). **c** Quantification of the infectious viral titres in the nasal turbinate and lung tissues of the SARS-CoV-1-infected mice ($n = 8$). **d** Viral N protein expression in the nasal turbinate and lung tissues of the SARS-CoV-1- infected mice ($n = 3$) at 3 dpi. was quantified with ImageJ. **e** Representative images of N protein expression (black arrow) in nasal turbinate and lung tissues of the SARS-CoV-1-infected mice. Scale bar represents 100 µm. **f** Histology analysis of the nasal turbinate and lung tissues of the SARS-CoV-1-infected mice by H&E staining. Black arrowhead, nasal epithelial desquamation; asterisk, hemorrhage in nasal submucosal region; dashed circle, necrotic cell debris in nasal cavity; open arrowhead, alveolar collapse; cross, inflammatory infiltration. Scale bar represents 200 µm. **g** Schematic illustration of MERS-CoV$_{MA}$ infection in hDPP4-knockin (hDPP4-KI) transgenic mice with vehicle or TMP1 treatment (Created in BioRender107). **h** Quantification of N gene of MERS-CoV$_{MA}$ in the nasal turbinate and lung tissues of the infected mice ($n = 5$). **i** Quantification of the infectious viral titres in the nasal turbinate and lung tissues of the MERS-CoV$_{MA}$-infected mice ($n = 5$). Each data point represents one biological repeat. Data represents mean ± SEM from the indicated number of biological repeats. Statistical significances were determined using two-tailed Student's *t*-test (**b**–**d**) and (**h**, **i**). Data were obtained from three independent experiments. * represented $p < 0.05$ and ** represented $p < 0.01$. Veh vehicle.

D614G mutation in the spike (Fig. 6g). We subsequently infected Calu3 cells with rSARS-CoV-2 NSP5-E166V, followed by TMP1 or NRV treatment. Expectedly, NRV treatment was ineffective against the recombinant virus ($EC_{50} > 50$ µM) (Fig. 6h). In sharp contrast, TMP1 dose-dependently decreased the intracellular viral gene copies of rSARS-CoV-2 NSP5-E166V in Calu3, resulting in an EC_{50} of 0.449 µM (Fig. 6h). We next asked whether antiviral efficacy of TMP1 against the NRV-resistant rSARS-CoV-2 was preserved in hACE2 transgenic mice. In concordance with the in vitro data, viral gene copies of rSARS-CoV-2 NSP5-E166V were reduced by TMP1 treatment in the nasal turbinate and lung tissues of the infected mice (Fig. 6i). Remarkably, infectious viral titres were decreased by 12.1- ($P = 0.003$) and 32.0-fold ($P = 0.0074$) by TMP1 treatment in the nasal turbinate and lung tissues, respectively (Fig. 6j). In comparison, infectious viral titres in the

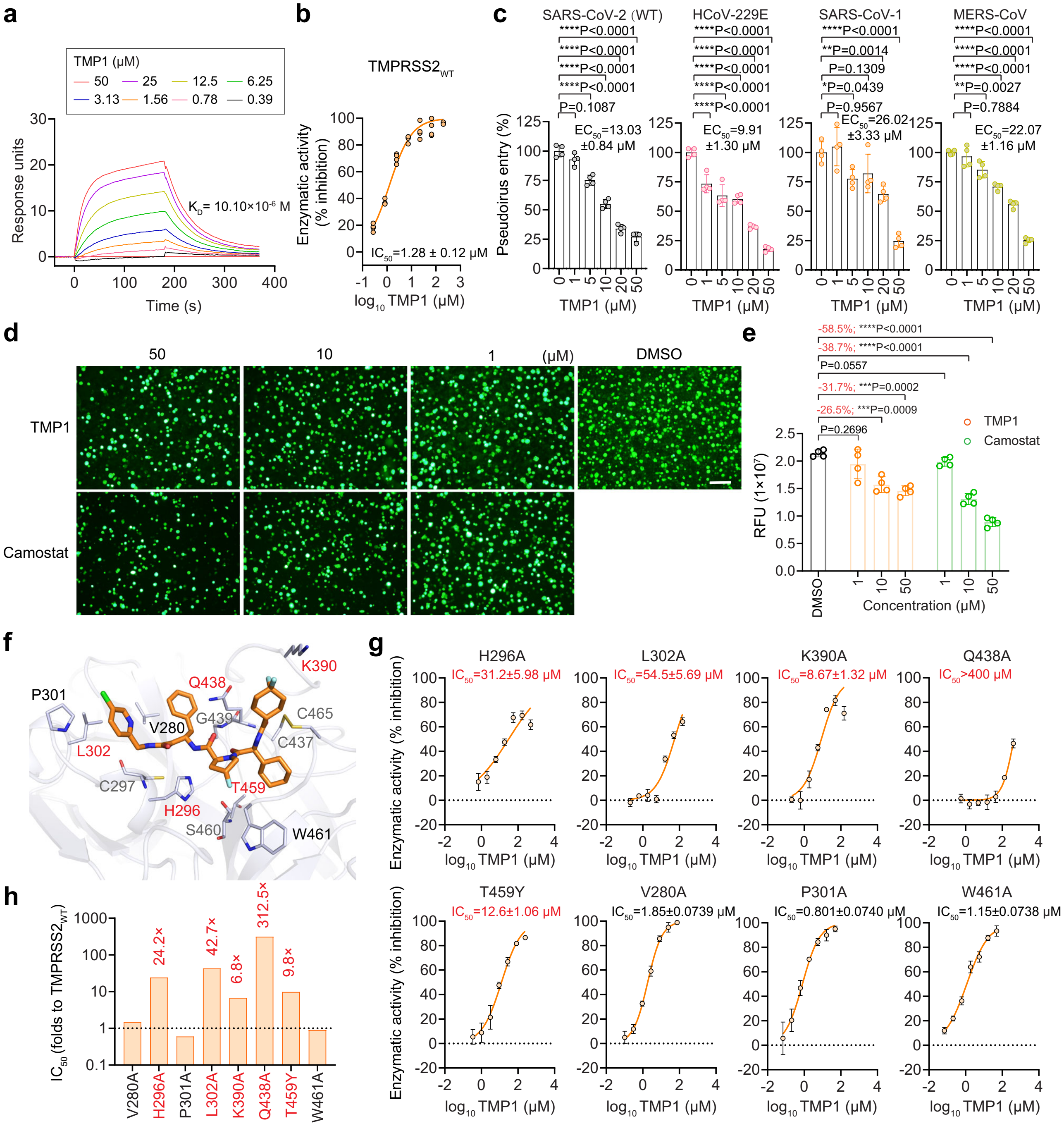

Fig. 5 | Specific inhibition of TMP1 against TMPRSS2 enzymatic activity and TMPRSS2-dependent pseudovirus entry. **a** Surface plasmon resonance (SPR) analysis of TMP1 with TMPRSS2. **b** Enzymatic activity of recombinant TMPRSS2 with TMP1 treatment ($n = 4$). **c** Inhibition of pseudovirus entry carrying different human coronavirus spikes by TMP1 treatment ($n = 4$). **d** Representative images of TMPRSS2-dependent cell-cell fusion. Scale bar represents 200 μm. **e** Quantification of the fluorescence signals of cell-cell fusion assays ($n = 4$) with ImageJ. RFU, relative fluorescence units. **f** Mode of binding between TMPRSS2 (blue-white) and TMP1 (orange). Key amino acids confirmed by mutagenesis assays (red) and hydrogen bonds (red dashed lines) were shown. **g** Enzymatic assays with TMPRSS2 mutants carrying key residues located in the TMP1-TMPRSS2 interaction interface ($n = 4$). **h** Fold change of change in IC_{50} of TMP1 against TMPRSS2 mutants compared with wildtype TMPRSS2. Each data point represents one biological repeat. Data represents mean ± SD from the indicated number of biological repeats. Statistical significances were determined using one way-ANOVA with Dunnett's multiple comparisons test (**c**) and (**e**). Data were obtained from three independent experiments. * represented $p < 0.05$ and ** represented $p < 0.01$, *** represented $p < 0.001$, **** represented $p < 0.0001$.

Paxlovid-treated mice nasal turbinates were 14.3-fold ($P = 0.0001$) higher than that of the TMP1-treated mice (Fig. 6j). In keeping with the infectious viral titres, only scarcely distributed viral antigen was found in the nasal turbinate of the TMP1-treated mice, while that of the vehicle- or Paxlovid-treated mice were extensively detected along the nasal epithelium (Supplementary Fig. 14a). Similarly, TMP1 treatment also reduced the N protein expression in the infected lung tissue samples when compared with the vehicle or Paxlovid treatment group (Supplementary Fig. 14a). Histological analysis further supported that the reduced viral burdens in the TMP1-treated mouse nasal turbinate and lung tissues led to alleviated virus-induced pathological changes (Supplementary Fig. 14b). Together, our mechanistic data indicates that TMP1 interacts with M^{pro} using a distinct mechanism when compared with NRV, therefore retaining the

Table 6 | Selectivity of the bispecific inhibitor against different human proteases

Host protease	Inhibition (%)	STD (%)	Concentration (μM)	Type	SI for M^{pro}	SI for TMPRSS2
Calpain 1	4.89	8.63	100	Cys	323	>78
Caspase-2	21.67	5.64	100	Cys	323	>78
Chymotrypsin	-14.65	22.65	50	Ser	161	>39
Cathepsin L	19.89	2.69	100	Cys	323	>78
Cathepsin D	0.66	2.03	100	Aps	323	>78
Neutrophil Elastase	6.37	1.14	100	Ser	323	>78
Thrombin	30.86	2.12	100	Ser	323	>78

Cys cysteine protease, *Ser* serine protease, *Aps* aspartic protease, *STD* standard deviation, *SI* selection index.

sensitivity against NRV-resistant SARS-CoV-2 escape mutants in vitro and in vivo.

In summary, our orally available bispecific inhibitor TMP1 simultaneously suppresses the activity of SARS-CoV-2 M^{pro} and host TMPRSS2, thus effectively blocking the infections and transmission of human-pathogenic coronaviruses.

Discussion

The continuous emergence of SARS-CoV-2 variants have imposed great challenges to antiviral therapy development. Monotherapy targeting a single viral protein is often associated with rapid emergence of escape mutations as we have seen in the clinical application of remdesivir[51,52] and Paxlovid[47,50,53]. Here, we described the discovery of a bispecific inhibitor TMP1 which simultaneously targeted the viral protease M^{pro} and the host protease TMPRSS2. We demonstrated the potent antiviral efficacy of TMP1 against wildtype SARS-CoV-2 and other variants of concern, including the prevalent Omicron JN.1 and KP.2 subvariants (Figs. 1 and 3). With side-by-side comparison with Paxlovid, we found both prophylactic and therapeutic treatment with TMP1 were comparably efficacious in protecting hACE2 transgenic mice from SARS-CoV-2 infection, thus ameliorating virus-induced tissue pathologies and lethality (Fig. 2). Interestingly, TMP1 not only inhibited the infection of SARS-CoV-2 but also protected against other human-pathogenic coronaviruses including the highly pathogenic SARS-CoV-1 and MERS-CoV (Figs. 1 and 4).

Priming of the spike protein by host proteases prior to fusion either at the plasma membrane or endosomes is essential for coronavirus entry. Therefore, a wealth of antiviral studies has targeted important host proteases such as TMPRSS2, cathepsin B/L and calpain[16,54–56]. Although coronaviruses can use a variety of host proteases to facilitate virus entry in cells with low or little TMPRSS2 expression, TMPRSS2-mediated membrane fusion remains as the dominant entry pathway utilized by coronaviruses for efficient virus entry in the human airway[10–13,20–22,25,26,57,58]. Therefore, we reasoned that targeting TMPRSS2 is physiologically relevant to the design of anti-coronavirus inhibitors. To this end, we performed stepwise chemical modifications to further optimized the anti-TMPRSS2 activity of our bispecific inhibitor (Fig. 1 and Table 1–4). To demonstrate the specific inhibition against TMPRSS2 in the context of coronavirus infection, we showed that TMP1 dose-dependently reduced the entry of pseudoviruses expressing spikes from a panel of human-pathogenic coronaviruses (Fig. 5) whose entry were previously shown to be TMPRSS2-dependent[10–12,20]. In parallel, TMP1 also inhibited TMPRSS-mediated cell-cell fusion (Fig. 5), which contributes to coronavirus spread and pathogenicity in vivo[25,26].

The beneficial role of TMPRSS2 inhibition against coronavirus infections was comprehensively evaluated by TMPRSS2-knockout mouse models[25,26] and by antiviral treatments with either conventional TMPRSS2 inhibitors like camostat and nafamostat[59,60] or other novel TMPRSS2 inhibitors both in vitro and in vivo[16,17,61]. Unfortunately, the most well-studied camostat and nafamostat used in clinical trials have shown rapid turnover into metabolites with significantly reduced bioactivity in vivo as demonstrated by others[9] and us (Fig. 2 and Supplementary Fig. 3), which substantially compromised their effectiveness in human patients[39,40,62–65]. Although a number of studies implicated a beneficial role of TMPRSS2 inhibitors in treating of COVID-19 patients, confounding factors such as insufficient patient number, heterogeneity of recruited patients, poor pharmacokinetic properties of the existing TMPRSS2 inhibitors, late patient presentation to antiviral therapy have obscured the assessment of the translational value of anti-TMPRSS2 antiviral therapy in clinical settings[63,66–71]. Therefore, these findings await to be further verified with a larger patient samples size. Collectively, design of TMPRSS2 inhibitors with higher potency and better bioavailability in vivo is warranted in the future.

As the first FDA-approved oral drug for COVID-19 treatment, Paxlovid has been widely used since first launched into the market[33]. However, its strong antiviral potency might be undermined by the emergence of NRV-resistant mutations[47,72,73]. Like the other classical peptidomimetic M^{pro} inhibitors[74–76], NRV acts by covalent binding with the enzymatic pocket of M^{pro}. In vitro virus passaging and recombinant virus experiments demonstrated T21I, L50F, E166A/V, S114A, ΔP168, A173V/T in the M^{pro} contributed to NRV resistance[48,53,72,73,77]. Alarmingly, among the clinical isolates identified with NRV resistance, E166V was found as the second most frequently-detected mutation in the M^{pro}, which contributed to 17.9% of NRV-resistant mutations[49,77]. In line with reports from others[47,53], we found that E166V most significantly reduced the sensitivity of SARS-CoV-2 M^{pro} to NRV (more than 200-fold increase in EC_{50}) (Fig. 6). Therefore, the need of developing alternative therapeutic options in combating NRV-resistance is warranted. Hinted by our crystallization analysis that TMP1 interacted with M^{pro} in a distinctive mode when compared to NRV, we verified that TMP1 remained highly potent against the M^{pro} carrying NRV-resistant mutations. Furthermore, TMP1 suppressed the replication of NRV-resistant recombinant SARS-CoV-2 in human lung cell lines and in transgenic mice (Fig. 6).

Combination therapy with antivirals targeting distinct virus or host proteins essential to the virus life cycle are invaluable because they enhance the treatment potency by synergistic inhibition and also reduce the emergence of drug-resistant mutant viruses, as exemplified by the highly active antiretroviral therapy (HAART) against human immunodeficiency virus (HIV) infection[78]. Synergistic anti-SARS-CoV-2 efficacy of the combination treatment with the orally available Paxlovid and Molnupiravir was recently reported in rhesus macaques[79], yet the potential benefits of combination treatment in humans needs to be further verified with randomized clinical trials. On the other hand, recent studies on the discovery of single antiviral molecules possessing dual-inhibition mechanisms further advanced the coronavirus antiviral research[54–56,80–86]. Since coronavirus M^{pro} and the host cathepsin L are both cysteine proteases that share structural similarity in the enzymatic pocket, majority of the dual-target inhibitors were discovered from screening of known M^{pro} inhibitors against the anti-cathepsin L activities[54,56,80–82]. However, given the indispensable role of TMPRSS2 in coronavirus entry in the human airways, we are the first study to simultaneously target coronavirus M^{pro} and TMPRSS2 by the bispecific inhibitor TMP1. Among the reported anti-coronavirus

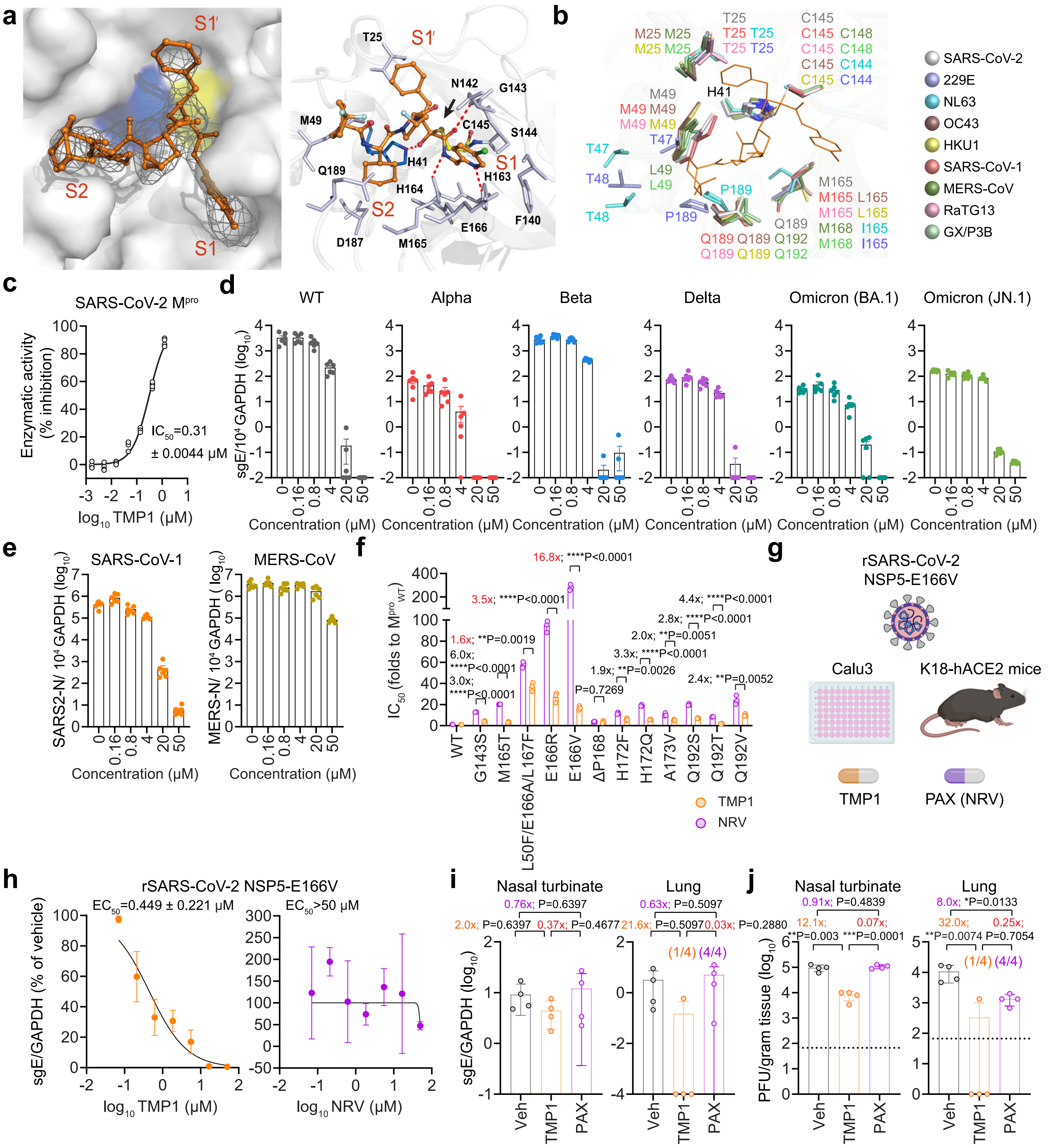

Fig. 6 | Specific inhibition of TMP1 against coronavirus M^{pro} and its antiviral efficacy against nirmatrelvir-resistant SARS-CoV-2 escape mutant. **a** Crystal structure of TMP1 (orange) in complex with SARS-CoV-2 Omicron M^{pro} (gray). The H41 (blue) and C145 (yellow) catalytic dyad, the S1′, S1, and S2 pockets of M^{pro} (red) and the *Fo-Fc* electron density map (gray mesh, $\sigma = 2.5$) were shown on left panel. Close-up view of the substrate binding pocket, the hydrogen bonds (red dashed lines) between TMP1 and the interacting amino acids, and the covalent-bond between C145 and TMP1 warhead (black arrow) were shown on right panel. **b** Superimposition of the TMP1 in complex with M^{pro} from 9 coronaviruses. **c** Enzymatic activity of recombinant SARS-CoV-2 M^{pro} with TMP1 treatment ($n = 4$). **d** Quantification of the sgE gene in VeroE6 cells ($n = 6$) infected with wildtype SARS-CoV-2 and Alpha, Beta, Delta, Omicron (BA.1 and JN.1) variants. **e** Quantification of the N gene of SARS-CoV-1 and MERS-CoV in infected VeroE6 cells ($n = 6$). **f** Sensitivity of recombinant SARS-CoV-2 M^{pro} mutants to TMP1 treatment ($n = 3$). **g** Schematic illustration of characterizing the in vitro and in vivo antiviral efficacy of TMP1 against nirmatrelvir-resistant recombinant SARS-CoV-2 (Created in BioRender)[108]. **h** Quantification of the sgE gene in Calu3 cells ($n = 3$) infected by rSARS-CoV-2-NSP5-E166V with nirmatrelvir or TMP1 treatment. **i** Quantification of SARS-CoV-2 sgE gene in the nasal turbinate and lung tissues of the rSARS-CoV-2-NSP5-E166V infected mice ($n = 4$) at 3 dpi. **j** Quantification of the infectious viral titres in the nasal turbinate and lung tissues of the rSARS-CoV-2-NSP5-E166V infected mice ($n = 4$) at 3 dpi. Each data point represents one biological repeat. Data represents mean ± SD from the indicated number of biological repeats. Statistical significances were determined using one way-ANOVA with Dunnett's multiple comparisons test (**i**, **j**) and two-tailed Student's *t*-test (**f**). Data were obtained from three independent experiments. * represented $p < 0.05$, ** represented $p < 0.01$, *** represented $p < 0.001$. Veh vehicle, NRV nirmatrelvir, PAX Paxlovid.

inhibitors with dual-target, in vivo antiviral potency was only available for four small molecules (GC376, Olgotrelvir, SMI141 and SMI142)[55,56,87]. In comparison with these M^{pro}/cathepsin L-targeting inhibitors, TMP1 showed improved animal survival against lethal coronavirus challenge, alleviated pathological changes in the infected tissues and strong capacity in blocking coronavirus transmission, therefore verifying the physiological importance of the antiviral targets selected in our current design.

In summary, we developed an orally available bispecific inhibitor TMP1 which simultaneously targets coronavirus M^{pro} and the host TMPRSS2. Virological assessment demonstrated the potent pan-coronavirus antiviral efficacy of TMP1 in vitro. Besides, TMP1 significantly ameliorated virus-induced lung pathology and rescued infected animals from lethal coronavirus infection, supporting its potential in preventing severe infection in patients which requires hospitalization. Overall, our research is a proof-of-concept study which shows simultaneous inhibition the coronavirus protease M^{pro} and the key host protease TMPRSS2 with one bispecific inhibitor represents a promising therapeutic strategy for treating coronavirus infections.

Methods

Ethics approval

The use of animals was approved by the Committee on the Use of Live Animals in Teaching and Research (CULATR) of The University of Hong Kong and the Institute Animal Care and Use Committee (IACUC) of West China Hospital, Sichuan University.

Virus and safety

WT SARS-CoV-2 HKU-001a (GenBank: MT230904), B.1.617.2/Delta (GenBank: OM212471), B.1.1.529/Omicron BA.1 (GenBank: OM212472), JN.1 (GISAID: EPL_ISL_18841631) and KP.2 (GISAID: EPI_ISL_19351035) were isolated from patients with laboratory-confirmed COVID-19 in Hong Kong[88]. MERS-CoV (GenBank: JX869059.2) was a kind gift from R. Fouchier (Erasmus Medical Center, Rotterdam, The Netherlands). HCoV-HKU1 (KF430198.1) was a kind gift from J. Zhao (Guangzhou Laboratory, China). The mouse-adapted MERS-CoV$_{MA}$ was a kind gift from P. McCray (University of Iowa, IA, USA). SARS-CoV-1 GZ50 (GenBank: AY304495), HCoV-229E (GenBank: PQ243243), HCoV-OC43, and HCoV-NL63 were archived clinical isolate at the Department of Microbiology, The University of Hong Kong (HKU). All variants of SARS-CoV-2 were cultured and titrated by plaque assays using VeroE6-TMPRSS2 cells. MERS-CoV and SARS-CoV-1 were propagated and titrated by plaque assays in VeroE6 cells. HCoV-229E was propagated and titrated by plaque assays in Huh7 cells. HCoV-HKU1, -OC43, and -NL63 were propagated in primary human airway organoids, MRC-5 and LLC-MK2 cells, respectively and titrated by one-step reverse transcription followed by quantitative polymerase chain reaction with specific primers listed in Supplementary Table 3. After obtaining the virus culture, the sequences of all variants used in this study were confirmed with nanopore sequencing. In vivo and in vitro experiments concerning live SARS-CoV-1, SARS-CoV-2, and MERS-CoV were performed according to the approved standard operating procedures of the Biosafety Level 3 facility at Department of Microbiology, HKU.

Cell lines

Huh7, VeroE6, and 293 T cells obtained from ATCC were maintained in Dulbecco's Modified Eagle medium (DMEM) supplemented with 10% heat-inactivated fetal bovine serum (FBS), 100 U/ml penicillin, and 100 µg/ml streptomycin (1% P/S). Calu3 cells obtained from ATCC were maintained in DMEM/F12 supplemented with 10% FBS, 1% P/S. VeroE6-TMPRSS2 cells were obtained from the Japanese Collection of Research Bioresources (JCRB) Cell Bank and cultured also in 10% FBS, 1% P/S DMEM and 1 mM (1%) sodium pyruvate.

Chemical synthesis and inhibitors used in vivo

TMP1 and its derivatives were synthesized in-house as described in Tables 1–4. Nirmatrelvir, camostat mesylate, 4-Hydroxy Benzeneacetic Acid 2-(Dimethylamino)-2-oxoethyl Ester (FOY-251) and ritonavir were purchased from MedChemExpress (USA, NJ, HY-138687, HY-13512, HY-19727A, HY-90001).

Animals

Heterozygous K18-hACE2 C57BL/6 J mice (2B6.Cg-Tg(K18-ACE2) 2Prlmn/J) were obtained from The Jackson Laboratory. The hDPP4 exon 10 to 12 KI mice were provided by P. McCray (University of Iowa, IA, USA) and were previously described[89,90]. Golden Syrian hamsters were obtained from the Centre for comparative Medicine Research of the University of Hong Kong. The BALB/c mice were obtained from Sichuan University. The animals were kept in cages with individual ventilation under 65% humidity and an ambient temperature of 21–23 °C and a 12–12 h day–night cycle for housing and husbandry. Food and water were provided to the animals without restriction. Group sizes were chosen based on statistical power analysis and our prior experience. Gender- and age-matched mice were randomized into different experimental groups.

Characterization of the in vitro toxicity of TMP1

VeroE6-TMPRSS2, VeroE6, Calu3, Huh7, MRC-5 and LLC-MK2 cells were treated with TMP1 diluted at the designated concentrations and incubated for 48 hpi. Cell viability was measured with luminescence-based CellTiter-Glo luminescent cell viability assay kit (G7573, Promega, WI, USA), following manufacturer's manual with the GloMax Explorer Multimode Microplate Reader (Promega). Luminescence signals are normalized with solvent controls.

Evaluation of in vitro antiviral activity

Calu3, VeroE6-TMPRSS2, VeroE6 or Huh7 cells were infected with SARS-CoV-2 (WT, Alpha, Beta, Delta, Omicron BA.1 or JN.1), recombinant SARS-CoV-2 NSP5-E166V, MERS-CoV, or HCoV-229E at multiplicity of infection (MOI) ranging from 0.01 to 2. Unless specified, cells were pre-treated with serially-diluted TMP1, nirmatrelvir or vehicle for 1 h prior to virus infection. DMSO-dissolved inhibitor stocks (10 mM) were diluted with culture medium to working concentrations. Final concentration of DMSO in the working solutions is 1%. Since VeroE6 cells were reported to highly express the efflux transporter P-glycoprotein (P-gp)[37], 2 µM CP-100356 was added as a specific P-gp inhibitor in antiviral assays conducted with VeroE6, VeroE6-TMPRSS2 and LLC-MK2 cells. Inhibitors were removed during virus infection by PBS washing for three times. After 2-hour incubation, the inoculum was removed and replaced with supernatants supplemented with inhibitors. Cells were incubated at 37°C until sample harvest.

RNA extraction and one-step reverse transcription-quantitative polymerase chain reaction (RT-qPCR)

Viral RNA was extracted from infected cells using QIAsymphony RNA Kit (931636, Qiagen, Germany). Viral RNA from mice lung and nasal turbinate samples were extracted with the RNeasy Mini kit (74106, Qiagen). After RNA extraction, RT-qPCR was performed using QuantiNova Probe RT-PCR Kit (208354, Qiagen) or QuantiNova SYBR Green RT-PCR Kit (208154, Qiagen) with the LightCycler 480 Real-Time PCR System (Roche). The primers and probes used in this study was included as Supplementary Table 3.

Virus titration with plaque assays

For organ harvested from infected animals, tissues were homogenized in DMEM with Tissue Lyzer II (Qiagen) and cleared supernatants are collected after centrifugation. To determine the infectious virus titre, supernatants from infected cells or organ tissues were ten-fold serially diluted and inoculated into monolayered VeroE6-TMPRSS2 cells (for quantification of SARS-CoV-1, SARS-CoV-2 and MERS-CoV) or Huh7 cells (for quantification of HCoV-229E) with 2 h incubation at 37 °C, followed by 1% low-melting point agarose overlay (16520050, Thermofisher, USA). The cells were further incubated for 48 h or 72 h before fixation with 4% formaldehyde for visualization with 0.5% crystal violet diluted in 25% ethanol/distilled water as previously described[91].

Air-liquid interface culture of primary human nasal epithelial cells (hNECs) and virus challenge in hNECs

The human nasal epithelial cells in air-liquid interface (ALI) culture were purchased from Epithelix (EP02MP, Epithelix, Switzerland) and maintained with MucilAir culture medium (EP04MM, Epithelix) until virus challenge. On the day of virus challenge, cells were pre-treated with or without TMP1 at the designated concentrations for 2 h, followed by virus inoculation at the apical side. Cells were incubated for 2 h at 37 °C to allow virus entry. Residual inoculum was removed and replaced with medium with or without TMP1. Apical supernatants and cell lysates were harvested for viral genome copy quantification by one-step RT-qPCR and infectious virus titration with plaque assays at 48 hpi.

Characterization of the toxicity of TMP1 in mice

Female 6- to 8-week-old K18-hACE2 transgenic mice were orally treated with 150 mg/kg/dose TMP1 or solvent only twice per day from day 0 to day 3. Blood was drawn from mice 24 h post the last dose of treatment and analysed for the concentration of aspartate transaminase (AST), alanine transaminase (ALT) and creatine (Cr) in the plasma according to the manufacturer's instruction (BC1555, BC1565 and BC4915, Solarbio, China). Body weight of the treated mice was measured daily. Histological analysis of major organ tissues harvested on day 14 post treatment.

Virus challenge with SARS-CoV-1, SARS-CoV-2 and MERS-CoV$_{MA}$ and drug treatment in mice

For SARS-CoV-2 infection, 8- to 12-week-old K18-hACE2 transgenic mice anaesthetized with 100 mg/kg ketamine and 10 mg/kg xylazine were intranasally inoculated with 1250 PFU or 500 PFU SARS-CoV-2 Delta variant. For SARS-CoV-1 infection hACE2 transgenic mice were challenged with 500 PFU SARS-CoV-1. For MERS-CoV infection, 8 to 12-week-old hDPP4-KI mice were challenged with 5000 PFU mouse-adapted MERS-CoV. For drug treatment, all drugs were formulated with 10% DMSO, 10% Kolliphor HS 15, 30% polyethylene glycol 400 (PEG 400) in normal saline. 20 mg/kg ritonavir was included in all oral treatment groups as pharmacokinetic enhancer. hACE2 transgenic mice were orally treated with 100 mg/kg/dose TMP1 or nirmatrelvir in combination with 20 mg/kg/dose ritonavir or vehicle only twice per day. For intranasal treatment, hACE2 transgenic mice were intranasally treated with 10 mg/kg/dose TMP1 or Analogue-TMPRSS2 ((2S,4 R)-N-((2 R)-4-((1-(benzo[d]thiazol-2-yl)-5-guanidino-1-oxopentan-2-yl)amino)-3,4-dioxo-1-phenylbutan-2-yl)-1-((S)-2-cyclohexyl-2-(4,4-difluorocyclohexane-1-carboxamido)acetyl)-4-fluoropyrrolidine-2-carboxamide) once per day. hDPP4-KI mice were orally treated with 150 mg/kg/dose TMP1 in combination with 20 mg/kg/dose ritonavir or vehicle only twice per day. For prophylactic therapy, treatment onset one day prior to virus infection while therapeutic treatment was delayed to 24 hpi. Nasal turbinate and lung tissues were harvested at 3 dpi. for virological assessment by RT-qPCR and plaque assays. For survival study, body weight and survival of the infected mice will be monitored for 14 days or until death of the animal, whichever was earlier.

Hamster transmission study

Transmission study was performed in golden Syrian hamsters as previously established[44,92]. 8- to 10-week-old female and male index hamsters were orally treated with 90 mg/kg/dose TMP1 in combination with 20 mg/kg/dose ritonavir twice on the day prior to virus challenge. At 0 dpi., hamsters were anaesthetized with standard 200 mg/kg ketamine and 10 mg/kg xylazine, followed by intranasal inoculation with 2000 PFU SARS-CoV-2 Delta strain. The index hamsters were rested for 16 h before being co-housed with the naïve hamsters for 5 h at 1 dpi. to allow contact transmission. Treatment for the index hamsters were continued twice per day until the end of virus transmission period at 1 dpi. Contact hamsters were then returned to single housing until sample harvest at 3 days post exposure (4 dpi.) for virological and histological assessments.

Immunohistochemistry (IHC) staining and histology analysis

IHC staining was performed to detect viral proteins from animal organ tissue samples. The nucleocapsid protein (NP) of MERS-CoV$_{MA}$ was detected by in-house guineapig polyclonal anti-MERS-CoV NP antibody and SARS-CoV-1 and SARS-CoV-2 was detected using in-house rabbit polyclonal anti-SARS-CoV NP antibody, followed by incubation with biotinylated rabbit anti-guineapig IgG (H + L) (ab6770, Abcam, UK) or biotinylated goat anti-rabbit IgG (H + L) secondary antibody (BA-1000, Vector laboratories, USA). Specificity of the inhouse primary antibody was validated as previously described[93,94]. The color development was carried out with VECTASTAIN® ABC-AP Kit and VectorRed substrate kit (AK-5000 and SK-5100, Vector Laboratories) according to the manufacturer's instructions. The nuclei counterstaining was performed by Gill's haematoxylin followed by mounting with Vectamount permanent mounting medium. For H&E staining, the tissue sections are stained with Gill's haematoxylin (H-3401-500, Vector Laboratories) and eosin-Y. All images are acquired by Olympus BX53 light microscope. IHC quantification was performed with IHC Image Analysis Toolbox as previously reported[22].

Pseudovirus package and entry assays

SARS-CoV-2-wildtype spike, SARS-CoV-1-spike, MERS-CoV-spike and HCoV-229E-spike pseudoviruses were packaged as previously described[95,96]. Briefly, 293 T cells were transfected with different spikes with Lipofectamine 3000 (L3000-015, Thermo Fisher Scientific). At 24 h post transfection, the cells were transduced with VSV-deltaG-firefly pseudotyped with VSV-G. At 2 h post transduction, the cells were washed three times with PBS and cultured in DMEM containing 1% FBS and anti-VSV-G (8G5F11) antibody (EB0010, Kerafast, MA, USA). The pseudoviruses were then harvested at 16 h post transduction and titrated with TCID$_{50}$ assays.

For pseudovirus entry assays, DMSO-dissolved TMP1 was diluted in DMEM containing 2% FBS to the designated concentrations resulting in 0.5% DMSO in the working solutions. Infection of peudoviruses carrying SARS-CoV-2-S was performed in VeroE6 TMPRSS2 cells. Infection of peudoviruses carrying SARS-CoV-1-S, MERS-CoV-S and HCoV-229E-S was performed in Huh7 cells. Cells were pre-treated with TMP1 for 2 h, followed by pseudovirus infection for 2 h. The cells were then incubated in an incubator (37, 5% CO$_2$) for 24 h, before being washed and lysed for detection of luciferase signal with a luciferase assay system (DD1204, Vazyme, China) according to manufacturer's instructions.

Cell-cell fusion assay with camostat and TMP1 treatment

Cell-cell fusion assay was adapted from a protocol as we previously described[95,97]. Briefly, 293 T cells were co-transfected with different SARS-CoV-2 wildtype spike plasmids with GFP1-10 plasmid (cat#68715, Addgene, USA) as effector cells. Another population of 293 T cells was co-transfected with ACE2, TMPRSS2, and GFP11 (cat#68716, Addgene) as target cells. After 24 h post-transfection, the target cells were treated with serially-diluted TMP1 or camostat for 1 h. For control wells, cells were treated with 0.5% DMSO in DEM. Effector and target cells were subsequently digested by EDTA–Trypsin (25200-072, Gibco) and mixed at a 1:1 ratio. The mixed cells were co-cultured at a 37 °C incubator for another 24 h. TMP1 and camostat were maintained in the supernatants during incubation. The co-cultured cells were fixed in 10% formalin and then permeabilized with 0.1% Triton-X100 (Sigma, USA) at room temperature. The antifade mounting medium with 4′,6-Diamidino-2-Phenylindole, Dihydrochloride (DAPI, H-1200, Vector Laboratories) was used for mounting and DAPI staining. Images were taken with the Olympus BX73 fluorescence microscope (Olympus Life Science, Tokyo, Japan).

Molecular docking of TMP1 against TMPRSS2 and M^{pro}

Molecular docking was implemented in the GOLD module with the GoldScore fitness function[98] using slow search settings. For docking of TMP1 with TMPRSS2, the receptor structure was taken from the protein data bank (PDB) (PDB entry: 7MEQ) and pre-processed, including filling in missing sidechains, removing waters, adding hydrogen atoms. Flexible docking was performed by defining the area within 10 Å around the 7MEQ ligand as binding site, and the amino acid sidechains of the binding site were set as flexible. All other parameters were set to default values.

For docking of TMP1 with coronavirus M^{pro}s, the protein structures of eight coronavirus main proteases were taken from PDB[99] including SARS-CoV-1 (PDB entry: 1WOF), MERS-CoV (PDB entry: 4RSP), NL63 (PDB entry: 7E6M) and 229E (PDB entry: 2ZU2), or from the AlphaFold Protein Structure Database (https://alphafold.ebi.ac.uk) including OC43 (GenBank: YP_009555250.1), HKU1 (GenBank: YP_173236.1), RaTG13 and GX/P3B. The genome sequences of RaTG13 (GISAID: EPI_ISL_402131) and GX/P3B (GISAID: EPI_ISL_410543) were downloaded from GISAID and translated to protein sequences. Then, those structures were pre-processed by filling in missing sidechains, removing waters, adding hydrogen atoms, and aligned to the SARS-CoV-2 main protease structure (PDB entry: 9IZB). Flexible docking was performed by defining the area within 8 Å around the 9IZB ligand (TMP1) as binding site, and the amino acid sidechains of the binding site were set as flexible. For each protein, the predicted pose of the ligand with the smallest root mean square error (RMSD) to TMP1 was selected as the binding pose. All other parameters were set to default values. The entire process of molecular docking was implemented in Discovery Studio 3.1.

Design and cloning of TMPRSS2 and its mutation constructs

The gene coding human TMPRSS2 (GenBank: KJ897688.1) was synthesized by the GENERAL BIOL, Anhui, China. The PCR fragment including TMPRSS2 ectodomain (residues 109-492) was amplified and inserted into the pFastBac1 vector using restriction sites *EcoRI* and *HindIII*, with a signal peptide GP64 (baculovirus envelope glycoprotein) at the N-terminus, and a 6×His tag at the C-terminus. The auto-activation sequence $_{250}$SRQSR$_{255}$ ↓ IVGGE (the arrow indicates the cleavage site) of TMPRSS2 was replaced with an enterokinase-cleavage sequence $_{250}$DDDDK$_{255}$. The eight mutations of TMPRSS2 (V280A, H296A, P301A, L302A, K390A, Q438A, T459Y, and W461A) were constructed using single-point mutation method. Plasmid transfer vector containing the wild-type or mutant TMPRSS2 ectodomain gene was transformed into *E. Coli* DH10Bac strain to generate recombinant viral Bacmid DNA. All primers are presented in Supplementary Table 4.

Protein expression, purification, and activation of wild-type and mutant TMPRSS2 ectodomain

Taken the wild-type TMPRSS2 ectodomain as an example, Sf9 cells were transfected with Bacmid DNA using LipoInsect™ transfection reagents (C0551, Beyotime Biotechnology, China), according to the manufacturer's instructions. After 96 h post-infection, P0 (about 2 mL) viral stock was collected and amplified to produce P1 to P3 (about 10 mL) viral stock. Two liters of sf9 cells cultured in the SIM SF Expression Medium (MSF1, Sino Biological, China) were infected with the P3 virus. TMPRSS2 ectodomain was then expressed and secreted outside cells at 27 °C under shaking at 110 rpm within 4-5 d after baculovirus infection.

Next, the supernatant of cell culture was collected by centrifugation with 7500 × *g*, at 4 °C, 10 min, to remove the cell pellet. Subsequently, the supernatant was incubated with 5 ml Ni-NTA with shaking at 110 rpm, 2 h, at 16 °C, and transferred to a gravity flow column. The protein bound to the Ni-NTA column was washed using TBS buffer (25 mM Tris, pH 8.0, 150 mM NaCl), then was eluted using TBS buffer plus 250 mM imidazole. The eluted sample was concentrated to about 2 mg/mL and dialyzed to the reaction buffer (25 mM Tris, pH 8.0, 150 mM NaCl, 2 mM $CaCl_2$). Enterokinase (C620031, Sangon Biotech, China) was added into the eluted sample, to activate the TMPRSS2 zymogen. Then, the C-terminal His-tag was removed using TEV protease. The sample was concentrated and loaded to the Superdex 75 gel filtration column in size-exclusion chromatography buffer (25 mM Tris, pH 8.0, 75 mM NaCl). Finally, the target protein was concentrated about 10 mg/mL and stored at -80 °C.

Fluorescence resonance energy transfer assay with recombinant M^{pro} and TMPRSS2

22.5 µL optimized concentration of recombinant protease was pre-incubated with 2.5 µL test compound in reaction buffer (M^{pro} and its mutants: 20 mM HEPES buffer, pH 6.5, 120 mM NaCl, 0.4 mM EDTA and 20% glycerol. TMPRSS2 and its mutants: 50 mM Tris, pH 7.5, 250 mM NaCl and 25% glycerol) at 96-well plates for 10 min. Followed by the addition of 25 µL 20 µM FRET substrate (M^{pro} and its mutants: MCA-AVLQSGFR-Lys (DNP) -Lys-NH2. TMPRSS2 and its mutants: Boc-QAR-AMC). The fluorescence signal was read at 320/405 nm (M^{pro} and its mutants) and 360/460 nM (for TMPRSS2 and its mutants) on the CLARIOstar microplate reader (BMG).

Surface plasmon resonance (SPR) analysis

SPR experiments were carried out using a Biacore 8 K SPR system (GE Healthcare). Recombinant TMPRSS2 was immobilized on a Series S CM5 chip by amine coupling until the SPR signal reached ~5,000 RU (resonance units) at a flow rate of 10 µL/min. Different concentrations of TMP1 were then passed through the CM5 chip through flow cells for 120 s followed by a 120-s dissociation phase at a flow rate of 30 µL/min. Background binding to blank immobilized flow cells was subtracted, and equilibrium dissociation constant (K_D) values were calculated using the 1:1 binding kinetics model built in Biacore 8 K Evaluation Software.

In vivo pharmacokinetics of TMP1, Paxlovid and camostat

All drugs were consisted with 10% DMSO, 40% PEG400, 10% Kolliphor HS 15 and 40% normal saline. Male BALB/c mice ($n = 3$ per group) were intravenously (i.v.) treated with 0.5 mg/kg TMP1 or orally (p.o.) with 100 mg/kg nirmatrelvir/TMP1 or 20 mg/kg camostat in combination treatment with 20 mg/kg ritonavir.

The expression and purification of SARS-CoV-2 Omicron variant M^{pro} and its mutants

The method for expressing and purifying the Omicron variant (BA.5, GenBank: OP054053) M^{pro} and its mutants is consistent with our previously described procedures[34,100]. In brief, the cDNA sequence was cloned into the pET-28b vector, within the M^{pro} cleavage-site at the N-terminus and the PreScission cleavage-site at the C-terminus. The cloned plasmid was expressed in *E.* coli BL21(DE3) cells, and cultured in LB with Kanamycin (50 µg/ml) at 37 °C. Upon reaching an optical density (600 nm) of 0.6-0.8, induction was carried out by adding 0.5 M IPTG (18 °C, 18 h). Cell pellets were resuspended in the buffer (20 mM Hepes pH 7.5, 500 mM NaCl, 10 mM imidazole, 0.5 mM PMSF and 10% glycerol), followed by lysis via high-pressure homogenization. Subsequently, the lysate was clarified through centrifugation (18000 rpm for 45 min at 4 °C), and the supernatant was loaded onto the His-Trap FF column (GE Healthcare) for purification. After the addition of PreScission protease to remove the His tag overnight, the protein was further purified using a Superdex 75 Increase 10/300 GL column (GE Healthcare).

Crystallization, data collection, phase determination, and refinement

The purified M^{pro} (~5 mg/mL) and TMP1 were mixed at a molar ratio of about 1:10 and incubated on ice for 2 h. The mixture was then centrifuged at 13,000 rpm for 10 min. The sitting-drop vapor-diffusion technique was utilized, incorporating 1 µL of M^{pro}-TMP1 mixture and 1 µL of the reservoir at a temperature of 291 K. Crystals of M^{pro}-TMP1 were observed under the condition: 0.2 M Magnesium chloride hexahydrate, 0.1 M Tris pH 8.5, 25% w/v PEG3350 at 18 °C for 1 week. The crystal was fished out and flash-cooled in liquid nitrogen.

The X-ray diffraction experiment for M^{pro}-TMP1 were collected at the BL18U1 beamline (wavelength = 0.97853 Å, temperature = 100 K) of the Shanghai Synchrotron Radiation Facility (SSRF). The obtained dataset was processed using *XDS*[101] and scaled with Aimless in *CCP4*[102]. Molecular replacement was then performed on M^{pro}-TMP1 structure using the M^{pro} (PDB ID: 7C7P) as an initial model. Model building was subsequently carried out using Coot and the refinement of the structure was performed using *PHENIX.refine*[103]. The final statistics of data collection and structural refinement are shown in Supplementary Table 5.

Construction of recombinant SARS-CoV-2 with nirmatrelvir resistance

The cDNA from ancestral SARS-CoV-2 (strain HKU-001a), assembled into the pSMART-BAC vector by seamless assembly (E2621S, NEB, USA), was used as the background to generate a D614G amino acid substitution in the S gene and a E166V substitution at NSP5 gene, respectively. The mutations were introduced into the pSMART-BAC by site-directed mutagenesis and confirmed by Sanger sequencing. The recombinant clones with mutant sites were transformed into BAC-Optimized Replicator v2.0 Electrocompetent Cells (60210-1, LGC Biosearch Technologies, UK), followed by plasmids extraction to acquire ultrapure and high quality of full-length cDNA clone. Infectious virus is recovered by transfection of VeroE6-TMPRS2 cells with 2.5 µg of the full-length cDNA clone using Lipofectamine 3000 (L3000015, Thermo Fisher Scientific). At 48 h post-transfection, the supernatant was used to inoculate VeroE6-TMPRSS2 cells for viral passage. The recombinant virus was sent to next generation sequencing to confirm the desired mutation and the absence of undesired mutations in the viral genome.

Graphic illustration

Schematic illustration images were created with Adobe Illustrator CC2018 and BioRender software (https://biorender.com/).

Statistical analysis

Statistical comparison between two experimental groups were performed with unpaired two-tailed Student's t-test. Comparison between three or more experimental groups was performed with one-way ANOVA or two-way ANOVA. The survival of animals was compared using the log-rank (Mantel-Cox) test. 50% inhibitory concentration (IC_{50}) and 50% effective concentration (EC_{50}) were calculated by simple nonlinear regression model and dose-response model in GraphPad Prism 8.0 software. Differences were considered statistically significant when $p < 0.05$. Data analysis was performed with GraphPad Prism v.8.0.

Reporting summary

Further information on research design is available in the Nature Portfolio Reporting Summary linked to this article.

Data availability

Coordinates and maps associated with data reported in this manuscript was deposited to the Protein Data Bank (PDB) with accession number 9IZB (https://doi.org/10.2210/pdb9izb/pdb). Source data are provided with this paper.

References

1. Corman, V. M., Muth, D., Niemeyer, D. & Drosten, C. Hosts and Sources of Endemic Human Coronaviruses. *Adv. Virus Res.* **100**, 163–188 (2018).
2. Zaki, A. M., van Boheemen, S., Bestebroer, T. M., Osterhaus, A. D. & Fouchier, R. A. Isolation of a novel coronavirus from a man with pneumonia in Saudi Arabia. *N. Engl. J. Med* **367**, 1814–1820 (2012).
3. Drosten, C. et al. Identification of a novel coronavirus in patients with severe acute respiratory syndrome. *N. Engl. J. Med* **348**, 1967–1976 (2003).
4. Chan, J. F. et al. A familial cluster of pneumonia associated with the 2019 novel coronavirus indicating person-to-person transmission: a study of a family cluster. *Lancet* **395**, 514–523 (2020).
5. Zhou, P. et al. A pneumonia outbreak associated with a new coronavirus of probable bat origin. *Nature* **579**, 270–273 (2020).
6. Lednicky, J. A. et al. Independent infections of porcine deltacoronavirus among Haitian children. *Nature* **600**, 133–137 (2021).
7. Vlasova, A. N. et al. Novel Canine Coronavirus Isolated from a Hospitalized Patient With Pneumonia in East Malaysia. *Clin. Infect. Dis.* **74**, 446–454 (2022).
8. Chan, J. F. et al. Altered host protease determinants for SARS-CoV-2 Omicron. *Sci. Adv.* **9**, eadd3867 (2023).
9. Hoffmann, M. et al. Camostat mesylate inhibits SARS-CoV-2 activation by TMPRSS2-related proteases and its metabolite GBPA exerts antiviral activity. *EBioMedicine* **65**, 103255 (2021).
10. Shirato, K., Kawase, M. & Matsuyama, S. Middle East respiratory syndrome coronavirus infection mediated by the transmembrane serine protease TMPRSS2. *J. Virol.* **87**, 12552–12561 (2013).
11. Belouzard, S., Chu, V. C. & Whittaker, G. R. Activation of the SARS coronavirus spike protein via sequential proteolytic cleavage at two distinct sites. *Proc. Natl Acad. Sci. USA* **106**, 5871–5876 (2009).
12. Bertram, S. et al. TMPRSS2 activates the human coronavirus 229E for cathepsin-independent host cell entry and is expressed in viral target cells in the respiratory epithelium. *J. Virol.* **87**, 6150–6160 (2013).
13. Milewska, A. et al. Entry of Human Coronavirus NL63 into the Cell. *J Virol* **92**, https://doi.org/10.1128/JVI.01933-17 (2018).
14. Shirato, K., Kawase, M. & Matsuyama, S. Wild-type human coronaviruses prefer cell-surface TMPRSS2 to endosomal cathepsins for cell entry. *Virology* **517**, 9–15 (2018).
15. Simmons, G. et al. Inhibitors of cathepsin L prevent severe acute respiratory syndrome coronavirus entry. *Proc. Natl Acad. Sci. USA* **102**, 11876–11881 (2005).
16. Shapira, T. et al. A TMPRSS2 inhibitor acts as a pan-SARS-CoV-2 prophylactic and therapeutic. *Nature* **605**, 340–348 (2022).
17. Mahoney, M. et al. A novel class of TMPRSS2 inhibitors potently block SARS-CoV-2 and MERS-CoV viral entry and protect human epithelial lung cells. *Proc Natl Acad Sci USA* **118**, https://doi.org/10.1073/pnas.2108728118 (2021).
18. Zhao, M. M. et al. Cathepsin L plays a key role in SARS-CoV-2 infection in humans and humanized mice and is a promising target for new drug development. *Signal Transduct. Target Ther.* **6**, 134 (2021).
19. Shirato, K., Kanou, K., Kawase, M. & Matsuyama, S. Clinical Isolates of Human Coronavirus 229E Bypass the Endosome for Cell Entry. *J. Virol.* **91**, https://doi.org/10.1128/JVI.01387-16 (2017).
20. Hoffmann, M. et al. SARS-CoV-2 Cell Entry Depends on ACE2 and TMPRSS2 and Is Blocked by a Clinically Proven Protease Inhibitor. *Cell* **181**, 271–280.e278 (2020).
21. Beumer, J. et al. A CRISPR/Cas9 genetically engineered organoid biobank reveals essential host factors for coronaviruses. *Nat. Commun.* **12**, 5498 (2021).
22. Shuai, H. et al. The viral fitness and intrinsic pathogenicity of dominant SARS-CoV-2 Omicron sublineages BA.1, BA.2, and BA.5. *EBioMedicine* **95**, 104753 (2023).

23. Liu, Y. et al. Lineage-specific pathogenicity, immune evasion, and virological features of SARS-CoV-2 BA.2.86/JN.1 and EG.5.1/HK.3. *Nat. Commun.* **15**, 8728 (2024).
24. Peacock, T. P. et al. The furin cleavage site in the SARS-CoV-2 spike protein is required for transmission in ferrets. *Nat. Microbiol* **6**, 899–909 (2021).
25. Iwata-Yoshikawa, N. et al. TMPRSS2 Contributes to Virus Spread and Immunopathology in the Airways of Murine Models after Coronavirus Infection. *J Virol* **93**, https://doi.org/10.1128/JVI.01815-18 (2019).
26. Iwata-Yoshikawa, N. et al. Essential role of TMPRSS2 in SARS-CoV-2 infection in murine airways. *Nat. Commun.* **13**, 6100 (2022).
27. Ziebuhr, J., Snijder, E. J. & Gorbalenya, A. E. Virus-encoded proteinases and proteolytic processing in the Nidovirales. *J. Gen. Virol.* **81**, 853–879 (2000).
28. Jin, Z. et al. Structure of M(pro) from SARS-CoV-2 and discovery of its inhibitors. *Nature* **582**, 289–293 (2020).
29. Yang, H. et al. Design of wide-spectrum inhibitors targeting coronavirus main proteases. *PLoS Biol.* **3**, e324 (2005).
30. Zhang, L. L. et al. Crystal structure of SARS-CoV-2 main protease provides a basis for design of improved α-ketoamide inhibitors. *Science* **368**, 409 (2020).
31. Anand, K., Ziebuhr, J., Wadhwani, P., Mesters, J. R. & Hilgenfeld, R. Coronavirus main proteinase (3CLpro) structure: basis for design of anti-SARS drugs. *Science* **300**, 1763–1767 (2003).
32. Qiao, J. et al. SARS-CoV-2 M(pro) inhibitors with antiviral activity in a transgenic mouse model. *Science* **371**, 1374–1378 (2021).
33. Owen, D. R. et al. An oral SARS-CoV-2 M(pro) inhibitor clinical candidate for the treatment of COVID-19. *Science* **374**, 1586–1593 (2021).
34. Quan, B. X. et al. An orally available M(pro) inhibitor is effective against wild-type SARS-CoV-2 and variants including Omicron. *Nat. Microbiol* **7**, 716–725 (2022).
35. Dai, W. et al. Structure-based design of antiviral drug candidates targeting the SARS-CoV-2 main protease. *Science* **368**, 1331–1335 (2020).
36. Fraser, B. J. et al. Structure and activity of human TMPRSS2 protease implicated in SARS-CoV-2 activation. *Nat. Chem. Biol.* **18**, 963–971 (2022).
37. Hoffman, R. L. et al. Discovery of Ketone-Based Covalent Inhibitors of Coronavirus 3CL Proteases for the Potential Therapeutic Treatment of COVID-19. *J. Med Chem.* **63**, 12725–12747 (2020).
38. Saunders, N. et al. TMPRSS2 is a functional receptor for human coronavirus HKU1. *Nature* **624**, 207–214 (2023).
39. Jilg, N. et al. One Week of Oral Camostat Versus Placebo in Nonhospitalized Adults With Mild-to-Moderate Coronavirus Disease 2019: A Randomized Controlled Phase 2 Trial. *Clin. Infect. Dis.* **77**, 941–949 (2023).
40. Breining, P. et al. Camostat mesylate against SARS-CoV-2 and COVID-19-Rationale, dosing and safety. *Basic Clin. Pharm. Toxicol.* **128**, 204–212 (2021).
41. Zheng, J. et al. COVID-19 treatments and pathogenesis including anosmia in K18-hACE2 mice. *Nature* **589**, 603–607 (2021).
42. Shuai, H. et al. Attenuated replication and pathogenicity of SARS-CoV-2 B.1.1.529 Omicron. *Nature* **603**, 693–699 (2022).
43. Winkler, E. S. et al. SARS-CoV-2 infection of human ACE2-transgenic mice causes severe lung inflammation and impaired function. *Nat. Immunol.* **21**, 1327–1335 (2020).
44. Chan, J. F. et al. Simulation of the clinical and pathological manifestations of Coronavirus Disease 2019 (COVID-19) in golden Syrian hamster model: implications for disease pathogenesis and transmissibility. *Clin Infect Dis.* https://doi.org/10.1093/cid/ciaa325 (2020).
45. Sia, S. F. et al. Pathogenesis and transmission of SARS-CoV-2 in golden hamsters. *Nature* **583**, 834–838 (2020).
46. Meng, B. et al. Altered TMPRSS2 usage by SARS-CoV-2 Omicron impacts infectivity and fusogenicity. *Nature* **603**, 706–714 (2022).
47. Iketani, S. et al. Multiple pathways for SARS-CoV-2 resistance to nirmatrelvir. *Nature* **613**, 558–564 (2023).
48. Kiso, M. et al. In vitro and in vivo characterization of SARS-CoV-2 strains resistant to nirmatrelvir. *Nat. Commun.* **14**, 3952 (2023).
49. Hu, Y. et al. Naturally Occurring Mutations of SARS-CoV-2 Main Protease Confer Drug Resistance to Nirmatrelvir. *ACS Cent. Sci.* **9**, 1658–1669 (2023).
50. Zhu, Y. et al. In vitro selection and analysis of SARS-CoV-2 nirmatrelvir resistance mutations contributing to clinical virus resistance surveillance. *Sci. Adv.* **10**, eadl4013 (2024).
51. Stevens, L. J. et al. Mutations in the SARS-CoV-2 RNA-dependent RNA polymerase confer resistance to remdesivir by distinct mechanisms. *Sci. Transl. Med* **14**, eabo0718 (2022).
52. Gandhi, S. et al. De novo emergence of a remdesivir resistance mutation during treatment of persistent SARS-CoV-2 infection in an immunocompromised patient: a case report. *Nat. Commun.* **13**, 1547 (2022).
53. Duan, Y. et al. Molecular mechanisms of SARS-CoV-2 resistance to nirmatrelvir. *Nature* **622**, 376–382 (2023).
54. Sacco, M. D. et al. Structure and inhibition of the SARS-CoV-2 main protease reveal strategy for developing dual inhibitors against M(pro) and cathepsin L. *Sci. Adv.* **6**, https://doi.org/10.1126/sciadv.abe0751 (2020).
55. Mondal, S. et al. Dual Inhibitors of Main Protease (M(Pro)) and Cathepsin L as Potent Antivirals against SARS-CoV2. *J. Am. Chem. Soc.* **144**, 21035–21045 (2022).
56. Mao, L. et al. Olgotrelvir, a dual inhibitor of SARS-CoV-2 M(pro) and cathepsin L, as a standalone antiviral oral intervention candidate for COVID-19. *Med* **5**, 42–61.e23 (2024).
57. Hou, Y. J. et al. SARS-CoV-2 Reverse Genetics Reveals a Variable Infection Gradient in the Respiratory Tract. *Cell* **182**, 429–446.e414 (2020).
58. Mykytyn, A. Z. et al. SARS-CoV-2 Omicron entry is type II transmembrane serine protease-mediated in human airway and intestinal organoid models. *J. Virol.* **97**, e0085123 (2023).
59. Li, K., Meyerholz, D. K., Bartlett, J. A. & McCray, P. B. Jr The TMPRSS2 Inhibitor Nafamostat Reduces SARS-CoV-2 Pulmonary Infection in Mouse Models of COVID-19. *mBio* **12**, e0097021 (2021).
60. Hoffmann, M. et al. Nafamostat Mesylate Blocks Activation of SARS-CoV-2: New Treatment Option for COVID-19. *Antimicrob Agents Chemother* **64**, https://doi.org/10.1128/AAC.00754-20 (2020).
61. Sun, Y. J. et al. Structure-based phylogeny identifies avoralstat as a TMPRSS2 inhibitor that prevents SARS-CoV-2 infection in mice. *J. Clin. Invest.* **131**, https://doi.org/10.1172/JCI147973 (2021).
62. Quinn, T. M. et al. Randomised controlled trial of intravenous nafamostat mesylate in COVID pneumonitis: Phase 1b/2a experimental study to investigate safety, Pharmacokinetics and Pharmacodynamics. *EBioMedicine* **76**, 103856 (2022).
63. Zhuravel, S. V. et al. Nafamostat in hospitalized patients with moderate to severe COVID-19 pneumonia: a randomised Phase II clinical trial. *EClinicalMedicine* **41**, 101169 (2021).
64. Hernandez-Mitre, M. P. et al. TMPRSS2 inhibitors for the treatment of COVID-19 in adults: a systematic review and meta-analysis of randomized clinical trials of nafamostat and camostat mesylate. *Clin. Microbiol Infect.* **30**, 743–754 (2024).
65. Tobback, E. et al. Efficacy and safety of camostat mesylate in early COVID-19 disease in an ambulatory setting: a randomized placebo-controlled phase II trial. *Int J. Infect. Dis.* **122**, 628–635 (2022).
66. Morpeth, S. C. et al. A Randomized Trial of Nafamostat for Covid-19. *NEJM Evid.* **2**, EVIDoa2300132 (2023).

67. Seccia, T. M. et al. RAndomized Clinical Trial Of NAfamostat Mesylate, A Potent Transmembrane Protease Serine 2 (TMPRSS2) Inhibitor, in Patients with COVID-19 Pneumonia. *J Clin Med* **12**, https://doi.org/10.3390/jcm12206618 (2023).
68. Ikeda, M. et al. Multicenter, single-blind, randomized controlled study of the efficacy and safety of favipiravir and nafamostat mesilate in patients with COVID-19 pneumonia. *Int J. Infect. Dis.* **128**, 355–363 (2023).
69. Ansarin, K. et al. Effect of bromhexine on clinical outcomes and mortality in COVID-19 patients: A randomized clinical trial. *Bioimpacts* **10**, 209–215 (2020).
70. Wannigama, D. L. et al. Early treatment with fluvoxamine, bromhexine, cyproheptadine, and niclosamide to prevent clinical deterioration in patients with symptomatic COVID-19: a randomized clinical trial. *EClinicalMedicine* **70**, 102517 (2024).
71. Redondo-Calvo, F. J. et al. Aprotinin treatment against SARS-CoV-2: A randomized phase III study to evaluate the safety and efficacy of a pan-protease inhibitor for moderate COVID-19. *Eur. J. Clin. Invest* **52**, e13776 (2022).
72. Zhou, Y. et al. Nirmatrelvir-resistant SARS-CoV-2 variants with high fitness in an infectious cell culture system. *Sci. Adv.* **8**, eadd7197 (2022).
73. Heilmann, E. et al. SARS-CoV-2 3CL(pro) mutations selected in a VSV-based system confer resistance to nirmatrelvir, ensitrelvir, and GC376. *Sci. Transl. Med* **15**, eabq7360 (2023).
74. Thanigaimalai, P. et al. Design, synthesis, and biological evaluation of novel dipeptide-type SARS-CoV 3CL protease inhibitors: structure-activity relationship study. *Eur. J. Med Chem.* **65**, 436–447 (2013).
75. Thanigaimalai, P. et al. Development of potent dipeptide-type SARS-CoV 3CL protease inhibitors with novel P3 scaffolds: design, synthesis, biological evaluation, and docking studies. *Eur. J. Med Chem.* **68**, 372–384 (2013).
76. Konno, S. et al. Design and synthesis of new tripeptide-type SARS-CoV 3CL protease inhibitors containing an electrophilic arylketone moiety. *Bioorg. Med Chem.* **21**, 412–424 (2013).
77. Moghadasi, S. A. et al. Transmissible SARS-CoV-2 variants with resistance to clinical protease inhibitors. *Sci. Adv.* **9**, eade8778 (2023).
78. Carpenter, C. C. et al. Antiretroviral therapy for HIV infection in 1996. Recommendations of an international panel. International AIDS Society-USA. *JAMA* **276**, 146–154 (1996).
79. Rosenke, K. et al. Combined molnupiravir-nirmatrelvir treatment improves the inhibitory effect on SARS-CoV-2 in macaques. *JCI Insight* **8**, https://doi.org/10.1172/jci.insight.166485 (2023).
80. Costanzi, E. et al. Structural and Biochemical Analysis of the Dual Inhibition of MG-132 against SARS-CoV-2 Main Protease (Mpro/3CLpro) and Human Cathepsin-L. *Int. J. Mol. Sci.* **22**, https://doi.org/10.3390/ijms222111779 (2021).
81. Hu, Y. et al. Boceprevir, Calpain Inhibitors II and XII, and GC-376 Have Broad-Spectrum Antiviral Activity against Coronaviruses. *ACS Infect. Dis.* **7**, 586–597 (2021).
82. Ma, X. R. et al. MPI8 is Potent against SARS-CoV-2 by Inhibiting Dually and Selectively the SARS-CoV-2 Main Protease and the Host Cathepsin L. *ChemMedChem* **17**, e202100456 (2022).
83. Yuan, S. et al. Targeting papain-like protease for broad-spectrum coronavirus inhibition. *Protein Cell* **13**, 940–953 (2022).
84. Wang, H. et al. Structure-based discovery of dual pathway inhibitors for SARS-CoV-2 entry. *Nat. Commun.* **14**, 7574 (2023).
85. Ciaglia, T. et al. Peptidomimetics as potent dual SARS-CoV-2 cathepsin-L and main protease inhibitors: In silico design, synthesis and pharmacological characterization. *Eur. J. Med Chem.* **266**, 116128 (2024).
86. Xie, X. et al. Structure-based design of pan-coronavirus inhibitors targeting host cathepsin L and calpain-1. *Signal Transduct. Target Ther.* **9**, 54 (2024).
87. Caceres, C. J. et al. Efficacy of GC-376 against SARS-CoV-2 virus infection in the K18 hACE2 transgenic mouse model. *Sci. Rep.* **11**, 9609 (2021).
88. Chu, H. et al. Comparative replication and immune activation profiles of SARS-CoV-2 and SARS-CoV in human lungs: an ex vivo study with implications for the pathogenesis of COVID-19. *Clin. Infect. Dis.* https://doi.org/10.1093/cid/ciaa410 (2020).
89. Li, K. et al. Mouse-adapted MERS coronavirus causes lethal lung disease in human DPP4 knockin mice. *Proc. Natl Acad. Sci. USA* **114**, E3119–E3128 (2017).
90. Hu, B. et al. Divergent trajectory of replication and intrinsic pathogenicity of SARS-CoV-2 Omicron post-BA.2/5 subvariants in the upper and lower respiratory tract. *EBioMedicine* **99**, 104916 (2023).
91. Chu, H. et al. Targeting highly pathogenic coronavirus-induced apoptosis reduces viral pathogenesis and disease severity. *Sci. Adv.* **7**, https://doi.org/10.1126/sciadv.abf8577 (2021).
92. Yuan, S. et al. Pathogenicity, transmissibility, and fitness of SARS-CoV-2 Omicron in Syrian hamsters. *Science* **377**, 428–433 (2022).
93. Chu, H. et al. Coronaviruses exploit a host cysteine-aspartic protease for replication. *Nature* **609**, 785–792 (2022).
94. Shuai, H. et al. Emerging SARS-CoV-2 variants expand species tropism to murines. *EBioMedicine* **73**, 103643 (2021).
95. Chu, H. et al. Host and viral determinants for efficient SARS-CoV-2 infection of the human lung. *Nat. Commun.* **12**, 134 (2021).
96. Chan, J. F. et al. Virological features and pathogenicity of SARS-CoV-2 Omicron BA.2. *Cell Rep. Med* **3**, 100743 (2022).
97. Hu, B. et al. Spike mutations contributing to the altered entry preference of SARS-CoV-2 omicron BA.1 and BA.2. *Emerg. Microbes Infect.* **11**, 2275–2287 (2022).
98. Jones, G., Willett, P., Glen, R. C., Leach, A. R. & Taylor, R. Development and validation of a genetic algorithm for flexible docking. *J. Mol. Biol.* **267**, 727–748 (1997).
99. Berman, H. M. et al. The Protein Data Bank. *Nucleic Acids Res* **28**, 235–242 (2000).
100. Huang, C. et al. A new generation M(pro) inhibitor with potent activity against SARS-CoV-2 Omicron variants. *Signal Transduct. Target Ther.* **8**, 128 (2023).
101. Kabsch, W. Xds. *Acta Crystallogr D. Biol. Crystallogr* **66**, 125–132 (2010).
102. Karplus, P. A. & Diederichs, K. Linking crystallographic model and data quality. *Science* **336**, 1030–1033 (2012).
103. Afonine, P. V. et al. Towards automated crystallographic structure refinement with phenix.refine. *Acta Crystallogr D. Biol. Crystallogr* **68**, 352–367 (2012).
104. Shuai, V. https://BioRender.com/l4qp6ea (2025).
105. Shuai, V. https://BioRender.com/9h119tg (2025).
106. Shuai, V. https://BioRender.com/ow2uzn7 (2025).
107. Shuai, V. https://BioRender.com/oq9v2zj (2025).
108. Shuai, V. https://BioRender.com/z8w8tq8 (2025).

Acknowledgements

Hin Chu acknowledges supports by funding from National Natural Science Foundation of China Excellent Young Scientists Fund (Hong Kong and Macau) (32122001); the General Research Fund (17118621, 17119122), Collaborative Research Fund (C7103-22G, C7060-21G), and Theme-Based Research Scheme (T11-709/21-N), the Research Grants Council of the Hong Kong Special Administrative Region; Health@InnoHK, Innovation and Technology Commission, the Government of the Hong Kong Special Administrative Region; Partnership Programme of Enhancing Laboratory Surveillance and Investigation of Emerging Infectious

Diseases and Antimicrobial Resistance for the Department of Health of the Hong Kong Special Administrative Region Government; Sanming Project of Medicine in Shenzhen, China (SZSM201911014); the High Level-Hospital Program, Health Commission of Guangdong Province, China; National Key Research and Development Program of China (projects 2021YFC0866100 and 2023YFC3041600); Emergency Collaborative Project of Guangzhou Laboratory (EKPG22-01); General Programme, Guangdong Provincial National Science Foundation, China (2023A1515012325, 2024A1515010848); the University of Hong Kong Li Ka Shing Faculty of Medicine Enhanced New Staff Start-up Fund; the University of Hong Kong Outstanding Young Researcher Award; the University of Hong Kong Research Output Prize (Li Ka Shing Faculty of Medicine); the Major Science and Technology Program of Hainan Province (ZDKJ202003); the research project of Hainan Academician Innovation Platform (YSPTZX202004); the Hainan Talent Development Project (SRC200003); the support from Dr. Gallant Ho on the Gallant Ho Outstanding Young Professorship, and the donations from Richard Yu and Carol Yu, May Tam Mak Mei Yin, Richard Yu and Carol Yu, the Shaw Foundation Hong Kong, Michael Seak-Kan Tong, Lee Wan Keung Charity Foundation Limited, Providence Foundation Limited (in memory of the late Lui Hac-Minh), Hong Kong Sanatorium and Hospital, Hui Ming, Hui Hoy and Chow Sin Lan Charity Fund Limited, The Chen Wai Wai Vivien Foundation Limited, Chan Yin Chuen Memorial Charitable Foundation, Marina Man-Wai Lee, the Hong Kong Hainan Commercial Association South China Microbiology Research Fund, Perfect Shape Medical Limited, Kai Chong Tong, Tse Kam Ming Laurence, Foo Oi Foundation Limited, Betty Hing-Chu Lee, Ping Cham So, and Lo Ying Shek Chi Wai Foundation. All donors and funding sources had no role in the study design, data collection, analysis, interpretation, or writing of the manuscript. Shengyong Yang acknowledges supports by National Key R&D Program of China (2023YFF1204905), the National Natural Science Foundation of China (T2221004, and 82130104), the New Cornerstone Science Foundation (NCI202338), Major Project of Guangzhou National Laboratory (GZNL2024A01005), and 1.3.5 project for disciplines of excellence, West China Hospital, Sichuan University (ZYGD23006). Jian Lei thanks the supports by funding from National Natural Science Foundation of China (82473844) and the National Key R&D Program of China (2022YFC2303701 and 2021YFF0702000). Huiping Shuai acknowledges supports by the National Natural Science Foundation of China (82302493), Guangdong Basic and Applied Basic Research Fund General Programme (2023A1515011891), the University of Hong Kong Li Ka Shing Faculty of Medicine Seed Fund for Basic Research for New Staff and the University of Hong Kong Research Output Prize (Li Ka Shing Faculty of Medicine). We also thank the staff from beamlines BL18U1 and BL19U1 at Shanghai Synchrotron Radiation Facility of the National Facility for Protein Science (Shanghai, China) for great support.

Author contributions

H.S., S.Yang. and H.C. conceived and supervised the research, and designed the experiments; S.Yang and G.Z. performed the drug design; G.Z. with the assistance of Z.F. and Z.X. performed the chemical synthesis; J.L., X.X. and X.D. performed gene expression, protein purification and crystallization experiments; H.S., C.Y., Y.H. L.D. and H.T.W. performed antiviral cellular assays and in vivo antiviral and transmission studies; H.S., C.Y. performed histological analysis and quantification; J.Q., M.Z. and L.D. performed in vitro and in vivo toxicity studies; L.W., L.D. and B.H. performed pseudovirus assays; H.S., J.H., H.L., D.W., J.S. and Y.P. performed antiviral assays in ALI-hNEC; H.S. and Y.L. performed fusion assays and quantification; H.S., L.W., Y.C., J.S., and Yang.W. performed recombinant virus construction and antiviral assays; J.Q. with the assistance of Y.C. performed library screening, enzymatic activity and inhibition assays, IC_{50} measurements and SPR assays; Yifei.W. and Y.Y. performed molecular docking and sequence alignment; H.S., J.Q., C.Y., Q.L., T.Z., H.Z.,, S.Yuan, J.Z., K.Y.Y., J.F.-W.C., C.X., J.L., S. Yang and H.C. analysed and discussed the data; H.S., J.Q., C.Y., J.L., S.Yang. and H.C. drafted and revised the manuscript.

Competing interests

The authors declare no competing interests.

Additional information

Supplementary information The online version contains supplementary material available at https://doi.org/10.1038/s41467-025-60832-z.

Correspondence and requests for materials should be addressed to Jian Lei, Shengyong Yang or Hin Chu.

Peer review information *Nature Communications* thanks Jun Wang, and the other, anonymous, reviewer(s) for their contribution to the peer review of this work. A peer review file is available.

Reprints and permissions information is available at http://www.nature.com/reprints

---

[1]State Key Laboratory of Emerging Infectious Diseases, Department of Microbiology, School of Clinical Medicine, Li Ka Shing Faculty of Medicine, The University of Hong Kong, and Pandemics Research Alliance Unit at The University of Hong Kong, Hong Kong Special Administrative Region, China. [2]Department of Biotherapy, Cancer Center and State Key Laboratory of Biotherapy, and National Clinical Research Center for Geriatrics, West China Hospital, Sichuan University, Chengdu, Sichuan, China. [3]Guangzhou Laboratory, Guangzhou, Guangdong Province, China. [4]Guangzhou Medical University, Guangzhou, China. [5]National Institute of Biological Sciences, Beijing, China. [6]Tsinghua Institute of Multidisciplinary Biomedical Research, Tsinghua University, Beijing, China. [7]GMU-GIBH Joint School of Life Sciences, The Guangdong-Hong Kong-Macao Joint Laboratory for Cell Fate Regulation and Diseases, Guangzhou Medical University, Guangzhou, China. [8]State Key Laboratory of Respiratory Disease, National Clinical Research Center for Respiratory Disease, Guangzhou Institute of Respiratory Health, the First Affiliated Hospital of Guangzhou Medical University, Guangzhou, China. [9]State Key Laboratory of

Emerging Infectious Diseases, School of Public Health, The University of Hong Kong, Hong Kong Special Administrative Region, China. [10]College of Veterinary Medicine, Henan Agricultural University, Zhengzhou, China. [11]Centre for Virology, Vaccinology and Therapeutics, Hong Kong Science and Technology Park, Hong Kong Special Administrative Region, China. [12]Department of Infectious Disease and Microbiology, The University of Hong Kong-Shenzhen Hospital, Shenzhen, Guangdong Province, China. [13]Academician Workstation of Hainan Province, Hainan Medical University-The University of Hong Kong Joint Laboratory of Tropical Infectious Diseases, Haikou, Hainan Province, China. [14]Department of Microbiology, Queen Mary Hospital, Pokfulam, Hong Kong Special Administrative Region, China. [15]Materials Innovation Institute for Life Sciences and Energy (MILES), HKU-SIRI, Shenzhen, China. [16]These authors contributed equally: Huiping Shuai, Jingxin Qiao, Chaemin Yoon, Guo Zhang, Yuxin Hou, Xiaoyan Xia, Lei Wang, Xinyue Deng. ✉e-mail: leijian@scu.edu.cn; yangsy@scu.edu.cn; hinchu@hku.hk